Division of Biomedical Engineering

Department of Human Biology

University of Cape Town

Investigating brain metabolite levels in adolescents living with HIV using atlas-based magnetic resonance spectroscopic imaging (MRSI)

In fulfilment of the requirements for the degree:

MSc in Biomedical Engineering

Sonam Maharaj (MHRSON005)

Supervisor: Dr Frances Robertson

Co-supervisor: Prof Ernesta Meintjes

15/05/2024

Declaration

I, Sonam Maharaj, hereby declare that the work on which this dissertation/thesis is based is my original work (except where acknowledgements indicate otherwise) and that neither the whole work nor any part of it has been, is being, or is to be submitted for another degree in this or any other university.

I empower the university to reproduce for the purpose of research either the whole or any portion of the contents in any manner whatsoever.

Signed by candidate

Signature: ……

Date: 15/05/2024

Acknowledgements

There are several people who I would like to acknowledge and thank for making this Master's dissertation possible. I would like to thank my supervisors Dr Frances Robertson and Professor Ernesta Meintjes for their support and guidance through this project. I am very grateful for the opportunity to work under your supervision and for the new skills you encouraged me to learn. Thank you too, Dr Robertson, for your assistance in the coding required for the processing pipeline and for your endless patience and willingness to answer my countless questions.

Special thanks to the National Research Foundation (NRF) and National Institute of Health (NIH) for providing financial support and making this project possible.

Thank you to my friends who were a constant source of light and laughter. Sharing this experience with you all made this process much less daunting. And to the new friendships I made at the MRI research lab, thank you all for your great advice and support.

Last but not least, I would like to express my gratitude to my family who supported me through this long and difficult journey. I appreciate my parents for their unwavering love and prayers, words of encouragement and belief in my abilities. Without their sacrifices, I would not be here. And thank you to my brother who never failed to put his work aside whenever I need help and for supporting me through stressful times. We did it!

Abstract

Deficiencies in brain function and structure have been linked to perinatally acquired HIV (PHIV) despite the introduction of antiretroviral therapy (ART). Current studies are predominantly based on single voxel magnetic resonance spectroscopy (MRS) in younger children, with inconsistent findings. We aimed to develop atlas-based pipelines for analysing MRSI data to examine whether there are differences in brain metabolite levels between adolescents with PHIV and uninfected controls.

The study participants were 165 adolescents, of whom 86 were adolescents living with HIV from the CHER trial and 79 were age- and sociodemographically- matched uninfected controls. They were scanned on a Siemens 3T Skyra scanner with the scanning protocol including a high-resolution T1-weighted structural MRI using a multi-echo magnetization-prepared rapid acquisition gradient echo (MEMPRAGE) sequence and volumetric MRSI using spiral-encoded localized adiabatic selective refocusing (LASER) CSI. LCModel was utilized to achieve spectral quantification for absolute metabolite concentrations and ratios to total creatine. The metabolites investigated include NAA, GPC, total creatine, glutamate + glutamine and myo-inositol. Oryx-MRSI software was adapted in MATLAB2020a to perform processing of 3D MRSI data through the reading of LCModel spectral data, metabolite map generation and registration to the structural image. Metabolite concentrations were averaged within the caudate and thalamus obtained via registration to the Harvard-Oxford subcortical structural brain atlas and compared between HIV and control groups. A voxel-wise comparison of NAA and GPC maps was also performed.

Using multiple linear regression models, elevated GPC concentration was observed in the left caudate (p = 0.01) and elevated myo-inositol in both the left (p = 0.03) and right thalamus (p = 0.03) in adolescents with PHIV compared to the uninfected controls at 15 years of age. Voxel-wise analysis revealed clusters of elevated GPC in adolescents with PHIV compared to the uninfected controls in the left and right thalamus, right putamen and left caudate.

Increased GPC, together with increased myo-inositol, observed in the caudate and thalamus are indicative of ongoing inflammation in adolescents with PHIV despite early ART initiation. Furthermore, the clusters identifying increased GPC using the voxel-wise approach show consistency between the different analysis approaches thus verifying the feasibility of the MRSI technique in this application.

Table of Contents

List of Tables

List of Figures

List of Abbreviations

AIDS	Acquired Immunodeficiency Syndrome
ANOVA	Analysis of Variance
ART	Antiretroviral Therapy
ART – 40W	Group on early ART for 40 weeks
ART – 96W	Group on early ART for 96 weeks
ART - Def	The deferred ART group
Asp	Aspartate
BBB	Blood Brain Barrier
BG	Basal Ganglia
cART	Combined Antiretroviral Therapy
CHER	Children with HIV Early Antiretroviral
CHESS	Chemical Shift Selective sequence
Cho	Choline
CNS	Central Nervous System
Cr	Creatine
CRLB	Cramer-Rao Lower Bound
CSD	Chemical shift displacement
CSF	Cerebral spinal fluid
CSI	Chemical shift imaging
DICOM	Digital Imaging and Communications in Medicine
EPI	Echo-planar imaging
EPSI	Echo-planar spectroscopic imaging
FOV	Field of view
FWHM	Full width half maximum
GABA	γ-amino-butyric acid
Gln	Glutamine
Glu	Glutamate
GM	Gray matter
GPC	Glycerol-phosphocholine
HAART	Highly Active Antiretroviral Therapy
HIV	Human Immunodeficiency Virus
Ins	Myo-inositol

IQR	Interquartile range
LASER	Localized adiabatic selective refocusing
LCModel	Linear Combination Modelling software
MEGA	Mescher-Garwood
MEMPRAGE	Multi-echo magnetization-prepared rapid acquisition gradient echo
MFGM	Mid-frontal Gray Matter
MIDAS	Metabolite Imaging and Data Analysis System
MNI	Montreal Neurological Institute
MRS	Magnetic Resonance Spectroscopy
MRSI	Magnetic Resonance Spectroscopic Imaging
NAA	N-acetyl-aspartate
NAAG	N-acetyl-aspartate-glutamate
NaN	Not a Number
NIfTI	Neuroimaging informatics technology initiative
NMR	Nuclear Magnetic Resonance
PCh	Phosphocholine
PCr	Phosphocreatine
PE	Phosphatidylethanolamine
PHIV	Perinatal HIV
PRESS	Point resolved spectroscopy
PWM	Peritrigonal White Matter
RF	Radiofrequency
ROI	Region of interest
SI	Spectroscopic Imaging
SLIM	Spectral localisation by imaging
SNR	Signal-to-noise ratio
SPM12	Statistical Parametric Modelling Software
STEAM	Stimulated echo acquisition mode
STI	Sexually Transmitted Infection
SVS	Single Voxel Spectroscopy
Tau	Taurine
VOI	Volume of interest
WM	White matter

1. Introduction

The Human Immunodeficiency Virus (HIV) is one of the world's most serious health and development challenges with approximately 39 million people living with HIV (UNAIDS, 2022b), of whom 7.6 million people are from South Africa (UNAIDS, 2022a). New HIV cases in children below the age of 15 have reduced from 14 000 in 2018 to 8 000 at the end of 2022. However, despite this reduction, 230 000 children are living with HIV and 4.1 million have been HIV-exposed (UNAIDS, 2022a), making South Africa the country with the highest HIV statistics globally.

HIV is a virus that principally infects the immune system, particularly lymphocytes and macrophages, which are responsible for fighting infections in the body and are important in the central nervous system (CNS) (Ellis, Calero and Stockin, 2009). As a result, an individual's ability to protect themselves against infections decreases, leading to increased vulnerability to such infections and diseases, and risk of developing acquired immunodeficiency syndrome (AIDS). HIV is classified as a sexually transmitted infection (STI) but can also be transmitted between people via other methods including vertical transmission from a pregnant mother to her child during pregnancy, delivery, or breastfeeding (Hoare *et al.*, 2014). This is also known as perinatal HIV (PHIV) transmission (Le Doaré, Bland and Newell, 2012). Virus infection through vertical transmission happens at a vital stage in the brain development of a child and can have a significant effect on the developing CNS (Hoare *et al.*, 2015).

Improvements in HIV treatment and care, most notably the introduction of combined antiretroviral therapy (cART) in 1996 (Ellis, Calero and Stockin, 2009) have shifted the worldwide paediatric HIV epidemic into a new stage. As a result of reduced mortality and morbidity rates, the number of children with PHIV on ART surviving to adolescence and adulthood is increasing (Sohn and Hazra, 2013; Willen *et al.*, 2017). Despite this decreased morbidity due to newer and aggressive ARTs, many children from earlier eras where less efficacious regimens were implemented have survived into adolescence and adulthood and may experience ongoing brain injury (Sarma *et al.*, 2014). Furthermore, due to their longer exposure to HIV, neurocognitive impairment has become more prevalent and can have a significant impact on quality of life, with implications for higher education, career training and reproductive health (Souza *et al.*, 2010). Even with viral suppression from a young age, children living with PHIV continue to demonstrate neurodevelopmental delay (Sherr *et al.*, 2014; Nichols *et al.*, 2015; Ananworanich *et al.*, 2016; Phillips *et al.*, 2018; Boivin *et al.*, 2019) as well as evidence of ongoing brain alterations on neuroimaging (Mbugua *et al.*, 2016; Randall *et al.*, 2017; Toich *et al.*, 2018). Although there is well-documented involvement of HIV with the brain in perinatally infected infants and children, further research and study is needed on the long-term neurological outcomes in the youth (Sarma *et al.*, 2014; Laughton *et al.*, 2018).

The period of adolescence is a time that needs social navigating and can be challenging for a typically developing child. It is marked by significant changes in psychological, social and physical development in addition to hormonal changes associated with puberty (Blüml *et al.*, 2013). When coupled with the status implications and increased responsibilities associated with HIV, adolescents living with such are at an even bigger risk. Delays or abnormalities in brain development can exacerbate the difficulties already experienced during adolescence, impacting quality of life. Despite early ART commencement, these children and adolescents continue to show signs of cognitive deficits related to HIV (van Wyhe *et al.*, 2021). Adolescence is viewed as a time with continued structural changes in brain association areas, allowing for the prolonged development of cognitive abilities such as cognitive control and social cognition. Due to this prolonged development, adolescents may be rendered particularly sensitive to certain interventions (Dumontheil, 2016). Additionally, the exact degree of impaired cognitive functioning in children and adolescents living with HIV is not fully established (Phillips *et al.*, 2016). Therefore, there is a need to understand the effects of perinatal HIV on the developing brain throughout childhood and adolescence.

Magnetic resonance spectroscopy (MRS) is a non-invasive method of measuring local brain metabolism which provides information on brain maturation from a biochemical perspective and insights into brain development and health. Metabolite abnormalities measured by MRS have been described in both the gray and white matter of children and adults living with HIV, and relate to neurological impairment severity (Keller *et al.*, 2004).

MRS studies to date mostly involve cross-sectional investigations of HIV infected youth. This can pose limitations as the neurodevelopment of the participants has not been followed since early in life. Furthermore, such studies often group results from a wide age range, for example 6 to 16 years of age (Hoare *et al.*, 2015). This limits interpretation of their findings as the brain typically undergoes a lot of change over this large age range. However, this study focuses on the specific time period of adolescence which allows insights into the effects and findings particular to this age group.

The Children with HIV Early Antiretroviral (CHER) trial was a randomised trial conducted in South Africa from 2005 to 2011 in which comparisons were made between early (age < 12 weeks) time-limited ART and deferred ART in asymptomatic HIV-infected infants. The infants were randomly assigned to one of three different treatment strategies: ART deferred (ART – Def), early limited ART for 40 weeks (ART – 40W) and early limited ART for 96 weeks (ART – 96W). Interim results from the CHER trial showed that early ART decreased disease progression and reduced mortality in infants with HIV, with superior clinical and immunological outcomes compared to deferred ART (Cotton *et al.*, 2013). A neurodevelopment sub study conducted on the CHER trial infants at 11 months reported notable

improvements in locomotor and general development scores in the early treatment group compared to the ART – Def group (Laughton *et al.*, 2018; van Wyhe *et al.*, 2021). A subset of children from the CHER trial were subsequently enrolled into a longitudinal neurodevelopment study and had neuroimaging and neurocognitive testing approximately every 2 years starting from 5 years of age.

A longitudinal MRS analysis was conducted by van Biljon *et al.* (2021) on the brain metabolite levels in the basal ganglia (BG), frontal gray matter (FGM) and peritrigonal white matter (PWM) in Cape Town-based children from the CHER trial at ages 5, 7 , 9 and 11 years. The findings indicated that, despite early ART initiation (all before 18 months of age), inflammation persists in these regions in children with HIV (van Biljon *et al.*, 2021).

HIV-related differences in metabolite levels in children from the CHER trial have previously been examined using single voxel spectroscopy (SVS) only, which limits us to looking at a particular part of the brain. However, magnetic resonance spectroscopic imaging (MRSI) is technique that allows for the acquisition of a wider volume with a higher spatial resolution within an acceptable scan time and, due to the detection of metabolic profiles from numerous spatial locations, an unbiased characterization of the complete investigated object can be obtained (De Graaf, 2007). Metabolite maps obtained via MRSI can be registered to an atlas to examine whether there are differences in brain metabolite levels in adolescents due to PHIV which could be an underlying cause of or lead to possible neurological delays or differences compared to uninfected adolescents.

This study, therefore, aimed to determine whether there are differing brain metabolite levels in early treated adolescents living with PHIV compared to uninfected adolescents, as measured with MRSI. To do this we compare different approaches that involve registering MRSI-derived metabolite maps to an atlas. For consistency with single voxel acquisitions in the same cohort, we use the caudate which is part of the BG as one of our regions of interest (ROIs), in addition to the thalamus. The approaches we use are:

1. Group comparison of metabolites averaged within atlas-based ROIs, namely the caudate and thalamus.
2. Voxel-wise between group comparison of metabolite maps in standard space.

Based on SVS findings reported by van Biljon *et al.* (2021) on the same cohort from age 5 to 11 years, we hypothesized that adolescents living with PHIV would display higher levels of Cho and Ins in the caudate and thalamus than the uninfected controls. In addition, we hypothesized that voxel-wise comparison would give results similar to those obtained using the atlas-based ROI method.

2. Background and Literature Review

2.1. Introduction to HIV and ART

HIV type 1 (HIV-1) can invade the CNS early post infection and primarily infects immune cells that are part of the subgroup called activated $CD4^+$ lymphocytes or T cells, which are essential in responding to foreign bodies and fighting infections. Thereafter, macrophages are secondarily infected. Both of these are cellular components of the immune system (Ellis, Calero and Stockin, 2009). HIV-1 must cross a selective diffusion barrier called the blood brain barrier (BBB) to penetrate the CNS. The BBB is essential in protecting the CNS against circulating pathogens and toxic molecules as well as controlling brain homeostasis (Lorin *et al.*, 2020). HIV follows a Trojan horse model to cross the BBB where diapedesis, the process in which blood cells pass through capillary walls, allows the transmigration of infected cells early during infection (Valcour *et al.*, 2012; Lorin *et al.*, 2020). It is well established that HIV replication prefers creating a local viral reservoir within microglial cells and macrophages leading to neuroinflammation which, in turn, contributes to neurocognitive dysfunctions (Lorin *et al.*, 2020). However, the exact timing and degree of CNS infection and injury or inflammation are inadequately understood due to sparse data captured at an early period before seroconversion has occurred (Valcour *et al.*, 2012).

HIV-1 contains some genetic diversity which is characterized by genetically defined subtypes or clades ranging from A to K as well as their recombinants (Gnanakaran *et al.*, 2007). These variants reflect those which are genetically more related to each other due to shared evolutionary ancestry and are often clustered within geographical regions due to founder effects. An example of this is clades C and J, both of which are prevalent in Central Africa, and exhibit genetic similarities. The reasons for different subtypes are the high mutation rate and recombination ability of the HIV-1 virus as well as the diverse backgrounds of infected populations which leads to great genetic diversity. Not only has this genetic diversity been a major factor in the global spread of HIV, but it has also posed concerns for diagnosis, treatment, prevention efforts and disease progression (Ellis, Calero and Stockin, 2009).

Many HIV neuroimaging studies have been performed in the global North, such as the USA and Europe, where HIV-1 clade B is most prevalent (Ellis, Calero and Stockin, 2009). However, in Africa, the most prevalent clade is HIV-1 clade C. This is of importance as the majority, approximately 90%, of children with PHIV live in low and middle-income countries and mainly sub-Saharan Africa, an area which receives less attention (Flynn and Abrams, 2019). These strains have been noted to have distinct structural differences which suggests they may elicit different effects (Gnanakaran *et al.*, 2007). Therefore, studies done on adolescents in high-income countries might not accurately represent the situation in South Africa. Furthermore, a striking finding is the lack of published data specific to the

adolescent age group (10-25 years), particularly from resource-constrained countries, which have the highest HIV prevalence (Laughton *et al.*, 2013). The limited studies that have been done in high-income countries where factors such as HIV strain, healthcare access and socioeconomic environments differ from those in low-income countries like South Africa. Therefore, as these differences can have a profound effect on the development of a child, there are limitations to using this information to represent the problem from a South African perspective.

Before the introduction of cART in 1995, approximately 50% of children living with PHIV died before two years of age (Newell *et al.*, 2004). In resource-poor settings, however, cART access has rapidly expanded since 2004 with 28-80% of treatment-eligible children having begun cART (Laughton *et al.*, 2013). The rate of PHIV transmission occurring not only during pregnancy but also during labour, delivery or breastfeeding foregoing any cART interventions ranges between 20 and 25% (Irshad, Mahdy and Tonismae, 2022; Salan *et al.*, 2023). This has subsided with the use of cART, which has provided dramatic improvements in the health and longevity of individuals with HIV through viral suppression and partial restoration of immune functioning (Ellis, Calero and Stockin, 2009).

The mechanism behind ARTs is that they interrupt various replication stages of HIV, thus reducing viral load allowing for immune system restoration (Arts and Hazuda, 2012). This suppression, along with preventing virus resistance, is achieved using at least two drugs that are categorised under different antiretroviral classes as part of the cART/HAART regime. The 5 main classes based on their resistance profiles and metabolic mechanisms are presented in Table 2.1 below.

Table 2.1: Summary of the 6 main ART classes and their mechanisms (Arts and Hazuda, 2012).

ART Class	**Mechanism**
Reverse transcriptase inhibitors	Prevent viral DNA replication by blocking reverse transcription
Integrase inhibitors	Prevent viral DNA from integrating into the host genome
Protease inhibitors	Inhibition of the formation of infectious viral proteins through the enzyme protease
Fusion inhibitors	Prevent the virus from binding onto the host cell
Coreceptor antagonists	Prevent host cell infection by blocking the binding of the virus to the coreceptor

Yet, most ARTs remain in the peripheral blood system. The BBB limits the movement of ARTs from the circulation into the CNS due to the BBB's unique structure and the presence of efficient efflux systems, resulting in lower effectiveness in the brain (Ene, Duiculescu and Ruta, 2011). This, along with their

removal from the brain parenchyma, allows HIV to invade the CNS early post infection and provides a compartment for replication due to suboptimal drug pressure (Ene, Duiculescu and Ruta, 2011; Lorin *et al.*, 2020). This compartment, also known as a viral reservoir, has the potential to cause neuronal and astrocytic dysregulation, inflammation and cell death (Nath, 2015; Mzingwane and Tiemessen, 2017). The degree of ART penetration into CNS has an influence on the extent of neurocognitive improvement (Ellis, Calero and Stockin, 2009). Therefore, it is important to begin ARTs as soon as possible to restrict HIV CNS infiltration and, subsequently, limit neuroinflammation and brain damage responsible for neurocognitive disorders (Ene, Duiculescu and Ruta, 2011; Lorin *et al.*, 2020).

CNS penetration is varied according to the specific drug used and has evolved through the years. Antiretroviral drugs have been classified based on a CNS penetration effectiveness (CPE) score which considers pharmacokinetic data, pharmacodynamics such as molecular weight and physiochemical properties (de Oliveira, 2015). The score ranges from 1 (low CNS penetration) to 4 (high CNS penetration). The participants from the CHER trial began ART at infancy with first-line ART consisting of daily zidovudine and lamivudine with lopinavir-r until 6 months. Second-line ART consisted of didanosine, abacavir and nevirapine or efavirenz. The corresponding CPE score of these drugs are highlighted in Table 2.2 (Borrajo *et al.*, 2021). As both of these regimes have combined CPE scores larger than 8, they can be classified as active cART and are effective in penetrating the CNS (Ghosh, Sarkar and Mitsuya, 2017).

Table 2.2: CPE score for certain antiretroviral drugs.

Antiretroviral Drug Class	**4 (Very Good)**	**3 (Good)**	**2 (Fair)**	**1 (Poor)**
Reverse Transcriptase Inhibitors	**Zidovudine** **Nevirapine**	**Abacavir** Efavirenz	**Didanosine** **Lamivudine**	Adefovir Tenofovir
Integrase Inhibitors		Elvitegravir Raltegravir		
Protease Inhibitors	Amprenavir-r Indinavir-r	Amprenavir **Lopinavir-r**	Atazanavir Fosamprenavir	Nelfinavir Ritonvair
Entry Inhibitors		Maraviroc Vicriviroc		Enfuvirfide

There are, however, other complications paediatric specialists are facing concerning HIV care such as diminishing efficacy of HIV regimens as a result of patients not adhering to medications or viral mutations (Willen *et al.*, 2017). Issues such as behavioural dysfunction, psychiatric illness and cognitive impairments have been found to persist despite decreasing encephalopathy rates. However,

prolonged HIV therapies and their negative effects on the brain and body are not well known (Willen *et al.*, 2017).

2.2. Brain development during adolescence and effect of HIV

Vertical transmission of HIV occurs at a critical stage of development when the rapidly-developing CNS is vulnerable to adverse effects (Hoare *et al.*, 2015). The effects of HIV on cognitive functioning range from being quite subtle to pervasive, with encephalopathy being the most serious manifestation along the spectrum (Phillips *et al.*, 2016). The study of typical brain development via MRI techniques has established that adult levels of total brain volume are reached at the end of childhood. Despite this, considerable region-specific changes in both brain function and structure are associated with the period of adolescence, resulting in unique patterns of brain behaviour and responses (Dumontheil, 2016). Neuroimaging has also shown that adolescents living with HIV experience significant neuronal microstructure damage (Phillips *et al.*, 2016) as well as altered neurometabolic levels (Van Dalen *et al.*, 2016). Additionally, in children with PHIV, white and grey matter volume have been found to be lower, with a larger amount of white matter (WM) hyperintensities (Cohen *et al.*, 2016). Such studies demonstrate CNS compromise that may be associated with impairment of global cognitive ability and functioning in children and adolescents with PHIV.

The marked behavioural changes from infancy to adolescence are reflected through both structural and functional maturational changes (Blüml *et al.*, 2013). During childhood, both the limbic and prefrontal regions are maturing, the former earlier than the latter. Changes in maturation are experienced in adolescence, with developmental imbalance between these two systems corresponding with alterations in both neurocognitive and behavioural outcomes (Laughton *et al.*, 2013; Willen *et al.*, 2017). The limbic system plays a crucial role in deciding rewards and negative reinforcement and processing social information and emotional experiences. The prefrontal region, which is responsible for planning, impulse control, and judgement, is still undergoing maturation through this period.

Therefore, as a result of the differences in developmental timing of these areas, in addition to HIV targeting multiple regions and circuitry associated with executive disorders, adolescents with PHIV and young adults are particularly at risk for deficits emerging later, despite effective viral suppression from a young age (Willen *et al.*, 2017; Boivin *et al.*, 2019). Correspondingly, increases in impulsivity and risk taking have been observed (Laughton *et al.*, 2013; Telzer *et al.*, 2013). A meta-analysis of 22 studies (Phillips *et al.*, 2016) concluded that HIV mainly affects the domains of processing speed, working memory and executive functioning in children living with PHIV between 6 and 18 years (Boivin *et al.*, 2019). Deficits of executive function in particular, have been associated with poorer mental and

physical health outcomes, as well as non-adherence and unemployment in PHIV adults (Gorman *et al.*, 2009; Willen *et al.*, 2017; Rowe *et al.*, 2023).

Despite the many studies done examining typical brain development and the underlying morphological changes associated with such, there is limited information on the biochemical levels and processes related to these morphological changes. This information is of importance as it provides insight into not only metabolic processes but also potential biomarkers underlying certain structural changes. Metabolites have been implicated in developmental processes from infancy to adolescence, with major metabolic changes being seen in the first few months of life (Blüml *et al.*, 2013). Although cortical gray matter (GM) increases during pre-adolescence have been observed (Giedd *et al.*, 1999), relatively stable metabolite levels were found during this age. (Blüml *et al.*, 2013).

Subcortical structures, such as the basal ganglia (BG), play a vital role in cerebral development and brain functionality such as memory processes, controlled movement, language, motivation and providing frontal lobe signalling pathways (Leisman, Braun-Benjamin and Melillo, 2014). Several cortical loops involving the prefrontal association cortex and limbic cortex for cognition, both of which are linked to characteristic adolescent behaviour as mentioned previously, run through the BG (Graybiel, 2004). It is, however, often the earliest and most HIV-affected regions of the brain and can become calcified without treatment due to the tendency of HIV to disrupt neurological substrates within these subcortical regions (Hoare *et al.*, 2014; Willen *et al.*, 2017). Despite the less severe BG abnormalities in the new ART era, HIV-related metabolite concentrations and structural differences continue to be reported (van Biljon *et al.*, 2021). Changes in WM maturation correlate with ongoing myelination with both its volume and organization developing well into adulthood (Holmes *et al.*, 2017). A study observing cerebral metabolism within HIV infected patients report inflammation of the BG, frontal and parietal lobes induced by HIV infection with the increased neuron loss in the BG (Qi *et al.*, 2015). Furthermore, the thalamus has been identified as a region vulnerable to HIV infection (Pfefferbaum *et al.*, 2012; Zahr *et al.*, 2020) .

The caudate and corpus collosum have also been identified as regions with the highest HIV concentrations due to their close proximity to the ventricles and, therefore, cerebral spinal fluid (CSF). This close CSF proximity allows for HIV-infected mononuclear cells to easily penetrate these structures, thus enabling higher HIV toxin concentrations (Thompson *et al.*, 2006; Randall *et al.*, 2017). A study investigating subcortical volumes in children with PHIV at age 5 found that immunocompromised children had larger caudate volumes bilaterally and suggests that the caudate is especially vulnerable to the existing immune state (Randall *et al.*, 2017).

2.3. Magnetic Resonance Spectroscopy (MRS)

Magnetic resonance spectroscopy (MRS) is a non-invasive method of measuring regional levels of certain brain metabolites which can serve as an indicator of structural changes, such as myelination and synaptic reorganization during childhood, as a result of underlying or preceding metabolic events and cellular changes (Mbugua *et al.*, 2016; Holmes *et al.*, 2017; van Biljon *et al.*, 2021). Furthermore, biochemical data can lead to the development of biomarkers for irregular developmental processes. Five primary metabolites measured through MRS and their corresponding clinical indication are shown in Table 2.3 (Blüml *et al.*, 2013; Rae, 2014). These metabolites are robustly measured when using standard MRS sequences and are involved in certain metabolic pathways essential for cellular functions within a developing brain (Blüml *et al.*, 2013).

Table 2.3: Summary of the primary metabolites and their clinical indication measured through MRS.

Metabolite	**Clinical Indication**
N-acetyl-aspartate (NAA)	Neuronal integrity (reflects neuronal mitochondrial function)
Glutamate/Glutamine (Glu/Gln)	Metabolic activity and neuronal integrity (important excitatory neurotransmitter)
Creatine (Cr)	Energy metabolism (measure of cellular energy levels)
Choline (Cho)	Membrane integrity and turnover (primarily in macrophages and microglia) due to neurodegeneration/inflammation
Myo-inositol (Ins)	Signal transduction (measures glial proliferation, cell transport and hormone-sensitive neuroreception)

These metabolites are typically of interest in MRS studies as they are involved in specific biochemical pathways essential for a developing brain's cellular functions such as myelination, glutamatergic neurotransmission and axonal elongation (Blüml *et al.*, 2013). Along with these metabolites, combinations of metabolites including total NAA (tNAA: NAA + N-acetyl-aspartate-glutamate (NAAG)), total creatine (tCr: Cr + phosphocreatine (PCr)), Glu + Gln and total choline (tCho: phosphocholine (PCh) + glycerophosphocholine (GPC)) are also relevant, as they can be measured with lower uncertainty than their individual components.

In MRS, NAA is the most abundant metabolite visible and is a key supplier of acetyl groups for lipid synthesis along with the related dipeptide NAAG (Bjartmar *et al.*, 2002). It undergoes cyclic activity with synthesis occurring within neuronal mitochondria followed by degradation into oligodendrocytes (Blüml *et al.*, 2013). As NAA is mainly stored in mature neurons and axons, its concentration is regarded as a surrogate measure of the density and/or number of mature or "adult-type" neurons

and axons. Therefore, neurological disorders where there is neuronal and axonal loss and injury are associated with decreases in NAA concentrations (Bjartmar *et al.*, 2002).

Within the brain, Glu is the main excitatory neurotransmitter generated and used by neurons in the CNS (Blüml *et al.*, 2013). Therefore, it is largely involved in various neural functions and mediates important processes such as memory, cognition, learning as well as motor and sensory processing (Daikhin and Yudkoff, 2000). Its precursor, Gln, aids in regulating levels of Glu and other amino acid neurotransmitters, γ-amino-butyric acid (GABA) and aspartate (Asp), through the Gln/Glu cycle. The complex spectral pattern of Glu as well as its overlap with Gln in MR spectra creates complications in its quantitation (Blüml *et al.*, 2013). Therefore, to overcome this, the robust sum of Glu and Gln is often analysed.

Cr can be consumed through diet but is also synthesized endogenously in the CNS from 3 different amino acids namely glycine, L-arginine and L-methionine (Braissant *et al.*, 2005). Within the brain, it is involved in the metabolism of adenosine triphosphate (ATP) which is the energy supply for all brain cells (Blüml *et al.*, 2013). PCr aids in storing energy and replenishes/maintains ATP levels by converting PCr to free Cr with both contributing to the Cr peak shown in MRS (Blüml *et al.*, 2013). Additionally, Cr is involved in the maintenance of membrane potentials, neurotransmitter release and ion gradient restoration. It has also been observed to be associated with axonal growth (Braissant *et al.*, 2005).

Similarly to Cr, Cho is also obtained through dietary intake but can also be synthesized *de novo* in the body through the methylation of phosphatidylethanolamine (PE) and is an essential nutrient grouped with B complex vitamins (Sanders and Zeisel, 2007; Zeisel and Da Costa, 2009; Blüml *et al.*, 2013). It is a precursor for phospholipid synthesis which is a vital component of cell membranes and, therefore, is associated with cell membrane turnover. Elevated tCho is considered indicative of increased cell membrane synthesis and turnover (Podo, 1999). As the inflammatory process involves changes in cell composition and turnover, elevated tCho suggests inflammation (Ruiz-Cabello and Cohen, 1992). Choline is also a marker of cell membrane signalling and a precursor to the neurotransmitter, acetylcholine (Sanders and Zeisel, 2007). It has also been shown to play vital roles in foetal brain and memory development and in decreasing defects in neural tube development (Zeisel and Da Costa, 2009).

The derivation of Ins is either through diet or synthesis by the kidneys (Blüml *et al.*, 2013). It is a precursor of inositol phospholipids found in cell membranes, a marker of glial cell proliferation and crucial in signal transduction events present in WM before active myelination (Blüml *et al.*, 2013). Furthermore, Ins plays an important role in regulating CNS cell volume as an osmolyte through calcium homeostasis and sodium transport (Fisher, Novak and Agranoff, 2002).

2.3.1. Principles of MRS

Both MRS and MRSI investigate biochemical tissue composition non-invasively using principles of nuclear magnetic resonance (NMR) where the behaviour of nuclear spins under the influence of external magnetic fields is exploited for biochemical analysis.

Single Voxel Spectroscopy (SVS)

When exposed to a strong static magnetic field (B_0), certain nuclei, such as hydrogen protons, absorb and re-emit radiofrequency (RF) pulses at a specific resonance frequency determined by the local magnetic environment (De Graaf, 2007). The rotational motion of nuclear spins in the B_0 field or frequency of precession is described by the Larmor frequency (ω_0) and is given by equation 1.

$$\omega_0 = \gamma B_0 \qquad (1)$$

Where γ represents the gyromagnetic ratio constant, a property specific to each nucleus and B_0 is the magnetic field strength measured in tesla (T). In the external B_0 field, a small excess number of nuclear spins align parallel rather that anti-parallel to the direction of B_0, producing a net longitudinal magnetization (M_0). The application of an RF pulse B_1 at the Larmor frequency rotates this longitudinal magnetization vector into the transverse plane, where the rotating magnetization can be detected by the induced signal in a receive coil. The behaviour of net nuclear magnetization can be described using the Bloch equations given by equation 2, 3 and 4. These equations express the motion of the M_x, M_y and M_z components of M in the presence of the B_0 and B_1 external magnetic fields as they return to thermal equilibrium with relaxation time constant T_1 (longitudinal relaxation) and T_2 (transverse relaxation) (De Graaf, 2007).

$$\frac{dM_x(t)}{dt} = \gamma\big(M_y(t)B_z(t) - M_z(t)B_y(t)\big) - \frac{M_x(t)}{T_2} \qquad (2)$$

$$\frac{dM_y(t)}{dt} = \gamma(M_z(t)B_x(t) - M_x(t)B_z(t)) - \frac{M_y(t)}{T_2} \qquad (3)$$

$$\frac{dM_z(t)}{dt} = \gamma\big(M_x(t)B_y(t) - M_y(t)B_x(t)\big) - \frac{M_z(t)-M_o}{T_1} \qquad (4)$$

The resonance frequency is also affected by the chemical environment, thus different hydrogen-containing metabolites resonate at slightly different frequencies resulting in a spectrum of distinct peaks. These frequency differences between peaks are characterized by the chemical shift, measured in parts per million (ppm) and are due to the shielding effect (α) from orbiting electrons. This shielding effect influences the effective magnetic field (B) and is represented by equation 5 (De Graaf, 2007).

$$B = B_0(1 - \alpha) \qquad (5)$$

The shielding affects the frequency of precession due to its proportional relationship to field amplitude and is described by equation 6:

$$v = (\frac{\gamma}{2\pi})B_0(1-\alpha) \quad (6)$$

SVS is an MRS technique in which a spectrum is acquired from a specific voxel and provides detailed information on the metabolite concentrations in the excited region. It uses frequency-selective RF excitation in the presence of a gradient to spatially localize the signal. This can be done using various pulse sequences such as point-resolved spectroscopy (PRESS) and stimulated echo acquisition mode (STEAM). In these cases, 3 RF pulses are used with orthogonal gradients in the x, y and z planes to define a voxel at the intersection and to remove unwanted signals that influence spectral quality and metabolite quantification (Govindaraju, Young and Maudsley, 2000; De Graaf, 2007). STEAM uses 3 90° pulses which allows clean voxel selection but can result in high signal loss. In the case of PRESS, a 'double spin-echo' approach is used which involves a 90°-180°-180° sequence. A better signal-to-noise ratio (SNR) is achieved due to the refocusing 180° pulses using PRESS, however, it cannot achieve echo times (TEs) as short as STEAM (De Graaf, 2007).

Magnetic Resonance Spectroscopic Imaging (MRSI)

MRSI extends the MRS principles by introducing phase-encoding gradients to spatially encode chemical shift (δ) information. This allows simultaneous acquisition of spectra from multiple spatial locations, generating a 2D or 3D array across the imaged volume. This enables the creation of maps representing the spatial distribution of various metabolites with the observed frequency (ω_{obs}) represented as follows:

$$\omega_{obs} = \omega_0 + \delta \quad (7)$$

Phase encoding is achieved using magnetic field gradients (G_x, G_y and G_z) and are applied before signal acquisition resulting in a linear variation in the resonant frequency along the phase encoding direction. This linear variation encodes spatial information which allows differentiation of signals at different positions within the imaging slice. An example of this in the x direction is shown in equation 8.

$$\phi(x) = \gamma x G_x t \quad (8)$$

Where ϕ is the spatially dependent phase shift, γ represents the gyromagnetic ratio constant, x is the spatial position relative to the gradient isocentre and t is the duration of the phase encoding gradient.

Volume localization in MRSI involves acquiring spatially resolved spectra from specific regions of interest within the imaging volume and is achieved using spatially selective RF pulses and encoding gradients. Techniques such as PRESS and STEAM, as previously mentioned, are predominantly used in

single-voxel applications, but are also used in MRSI to select rectangular volumes (De Graaf, 2007). However, 3D localization in both single voxel spectroscopy and MRSI can also be done using LASER which utilises slice-selective adiabatic RF (AFP) pulses for both excitation and refocusing. The AFP pulses rotate magnetization efficiently across a range of resonant frequencies thus enabling wide spatial selection. The entire sample is excited after which 3 AFP pulse pairs selectively refocus 3 orthogonal slices to achieve 3D localization. LASER is favourable compared to spin-echo PRESS and STEAM due to its adiabatic property and ability to employ high bandwidth pulses. Due to these high bandwidth pulses, localization is very well-defined in terms of edge sharpness and chemical shift displacement is minimised (De Graaf, 2007).

Spatial Fourier transformations are used to convert spatially encoded data into the spatial frequency domain. This differs from typical MRS techniques in which only temporal Fourier transforms are used for spectral analysis. MRSI typically involves long acquisition times, but methods have been developed to overcome this limitation. The focus has shifted from k-space sampling reduction to the efficiency of k-space sampling with techniques such as echo-planar spectroscopic imaging (ESPI) and spiral encoding (De Graaf, 2007). EPSI combines principles from echo-planar imaging (EPI), which acquires multiple spatial locations during one readout period with short echo spacing, and spectral encoding (De Graaf, 2007). Its most common application is whole-brain MRSI due to its time-efficiency (Maudsley *et al.*, 2010). Compared to the zig-zag k-space trajectory produced in EPSI (Mansfield, 1984), spiral-encoding employs spiral k-space trajectories allowing for continuous and rapid k-space sampling of the entire plane with higher resolution and SNR (De Graaf, 2007; Bogner, Otazo and Henning, 2021).

Despite the high spectral quality and spatial resolution obtainable through MRSI, there are some limitations to this technique. These include chemical shift errors, B_1 field inhomogeneities and inadequate selection profiles which all lead to localization artifacts during scanning. Additionally, in standard MRSI, long scan times can result in limited spatial coverage and increase the likelihood of motion-induced artifacts (Bogner *et al.*, 2014). Therefore, to combat these limitations, improved MRSI sequences have been developed, namely the spiral-accelerated and LASER localised MRSI acquisition technique with real-time motion and B_0 correction. This has been shown to significantly improve spectral quality and localization accuracy even when strong motions during acquisitions were present (Bogner *et al.*, 2014). However, point spread functions and partial volume effects that may still occur during MRSI can be diminished using another MRS technique called spectral localization by imaging (SLIM).

SLIM is an alternative technique that is able to account for partial volume effects while estimating metabolite concentrations from homogenous ROIs using non-Fourier transformation (An, Warach and Shen, 2011; Goryawala *et al.*, 2018; Bogner, Otazo and Henning, 2021). This method acquires MR spectra through compartmentalization of arbitrary tissue shapes rather than rectangular voxels used in conventional MRS techniques (Lee, Adany and Choi, 2017) by using information from high resolution structural images to solve an over-determined system of equations (De Graaf, 2007; Goryawala *et al.*, 2018). As it is non-Fourier based, the spectra are precise recreations of the areas that have been compartmentalised as opposed to estimations associated with Fourier transformations methods such as MRSI (Ellis, Yang and Fischer, 2019). Comparisons have been made between MRSI and SLIM methods with the latter showing vast improvements in inter-voxel signal contamination (Adany, Choi and Lee, 2016; Ellis, Yang and Fischer, 2019).

Advantages of the SLIM theory is that it promises to allow compartmental signal localization using fewer k-space acquisitions. This is through utilizing prior information from high resolution MRI to reconstruct anatomical compartment spectra. However, a key limitation is the assumption that each compartment has spatial uniformity which defies the inhomogeneity of the B_0 and B_1 fields within a VOI beyond theoretical applications. This is especially significant when working with the brain due to its complex and convoluted anatomy (Khalidov *et al.*, 2006; Adany, Choi and Lee, 2016). To overcome this limitation, extensions to the original SLIM algorithm have been developed, namely the B-SLIM or BASE-SLIM methods (Khalidov *et al.*, 2006; Lee, Adany and Choi, 2017). The former corrects for B_0 inhomogeneity, however, uncorrected residual inhomogeneities remain due to the convoluted brain geometry. Therefore, BASE-SLIM is a B_0 -adjusted and sensitivity encoded SLIM extension and incorporates inhomogeneity information from both B_0 and B_1 fields, addressing the compartmental inhomogeneity restraint of SLIM (Lee, Adany and Choi, 2017).

2.3.2. Analysis of MRSI

Multivoxel MRS methods are imaging-based localization methods and are interchangeably called by the names MRSI, chemical-shift imaging (CSI) or simply spectroscopic imaging (SI) (Lee, Adany and Choi, 2017). MRSI is a powerful non-invasive tool allowing the study of spatially heterogeneous biochemical changes underlying several brain pathologies (Bogner *et al.*, 2014). When utilized *in vivo*, MRSI can be used to create distributions maps of various metabolites and, thus, possibly indicate regions of altered metabolism even when no structural changes are present (Maudsley *et al.*, 2006).

Thus far, the main approaches adopted for MRSI data analysis of brain neurochemicals have been categorized into three groups (Ma *et al.*, 2021):

1. Manually selecting voxels from a portion of the ROI to represent the entire region's neurochemical levels.
2. Atlas-based techniques in which MRSI data is interpolated and registered to a structural image (atlas) and voxels within an atlas- defined ROIs are averaged.
3. A voxel-based analysis through the registration of metabolite maps to a standard space to conduct a voxel-by-voxel statistical analysis, a similar approach utilized to analyse functional MRI data but not widely used in MRSI.

There are some drawbacks and limitations to each approach. Method 1 requires manual interaction which may present variations dependent on the user as well as time and training requirements. In MRSI techniques where millimetre level resolution can be achieved, methods 2 and 3 are better suited to providing group or statistical information on the metabolite levels in particular brain structures (Ma *et al.*, 2021). Maudsley *et al.* (2010) demonstrated the use of MRSI to acquire proton spectra from a large brain region, applying a processing method that is fully automated. Their findings show differences between subjects that are comparable to similar studies done on more limited brain regions. Such differences were found to only be slightly larger than those obtained from using single-voxel methods. Additionally, acquiring volumetric MRSI data and a corresponding water reference allowed the application of spatial normalization methods so that a voxel-based statistical analysis technique could be used across many subjects (Maudsley *et al.*, 2010).

However, spatial resolution in MRSI is typically rather low compared to imaging, with *in vivo* voxel sizes of approximately 1 x 1 x 1 cm^3 in humans (Kirchner *et al.*, 2015), similar to those used in the study by Ma *et al.* (2021). This is disadvantageous as it leads to voxel bleeding where the spectrum in a certain voxel exhibits contributions from other spatial regions (Kirchner *et al.*, 2015). It is not always noticeable, therefore, uncontrollable and unrecognizable signal spread can be ruinous to metabolite quantification with high specificity and spatial resolution (Kirchner *et al.*, 2015).

Another important consideration in MRSI is spectral fitting. Along with lipid contamination, B_0 inhomogeneity and poor water suppression, automatically generated metabolite maps derived from MRSI spectra can also be degraded through spectral fitting inaccuracies (Wilson *et al.*, 2019). To perform these tasks, many software packages have been developed such as LCModel (Provencher, 2001), MIDAS (Maudsley *et al.*, 2006) and TARQUIN (Wilson *et al.*, 2011) to name a few. Despite there not being a clear consensus on what algorithm is preferred for all cases, a common feature of the methods employed by different software packages is the utilisation of a quantum mechanically simulated or experimentally acquired set of metabolite spectra, also known as a basis set, into the fitting procedure. It is recommended to use this method over spectral integration or a single peak

modelling as there is a significant reduction in the total number of model functions needed to model the spectrum fully, thus, leading to fewer parameters requiring to be fit (Near *et al.*, 2021). Additionally, greater levels of prior knowledge of the fitting process is included in simulated basis sets (Wilson *et al.*, 2019). To ensure spectral fitting has been performed accurately, the quality of the individual spectra and their fit should be assessed. The standard visual assessment used in SVS is often impractical in MRSI due to the large number of spectra acquired. However, it is still advisable to perform this visual assessment in key diagnostic locations. The Cramer-Rao Lower Bound (CRLB) is a lower estimate of the concentration measurement error influenced by linewidth, SNR and mutual signal overlap and is an accepted numerical quality estimation (Wilson *et al.*, 2019).

In a study conducted by Ma *et al. (*2022), a new atlas-based brain-structure specific MRSI analysis approach was demonstrated in which neurochemical levels are regionally quantified in a subject's native image space by registering segmented masks of the structures of interest to interpolated neurochemical maps. In this way, average brain-structure specific metabolite concentration levels are obtained. This method was compared to the conventionally used approach of averaging over 4 manually selected MRSI voxels as well as the average of metabolite levels within a region represented by an SVS acquisition. All these methods were compared to the concentrations obtained using SVS within the same area. Excellent correlation was observed between different MRSI processing methods, suggesting minimal errors were introduced by moving from manual voxel selection to either automated method, both of which included interpolated metabolite map registration. The atlas-based approach produced better intra-subject test-retest reproducibility than manually selecting MRSI voxels (Ma *et al.*, 2021).

Ma *et al.* (2021), however, did not consider the point spread function for MRSI, did not acquire a water reference to apply water scaling, and did not consider partial volume effects resulting from differing proportions of GM, WM and CSF within an ROI, which confound regional estimation of brain metabolites. Partial volume effects are particularly evident when considering smaller brain regions (Goryawala *et al.*, 2018) and analysis methods can be extended to incorporate information on the tissue volume fraction in each voxel so that contributions from different tissues or regions can be separated.

2.3.3. MRS and MRSI in PHIV

In SVS, metabolite spectra are obtained from a single volume of interest (VOI) (Lee, Adany and Choi, 2017). According to Keller *et al.* (2004), metabolite abnormalities measured by MRS have been described in both the gray and white matter of HIV-infected children and adults. Furthermore, such abnormalities correlate with neurological impairment severity and can be improved through ART.

Metabolic maturation of the brain from birth through adolescence was analysed using MRS in a study done by Blüml *et al.* (2013). It was observed that the most significant changes in metabolite levels occur during the first 2 years of infancy. This is of great importance as it is a time of critical and rapid brain development and , therefore, is the period when the developing brain is most vulnerable to HIV infection (Mbugua *et al.*, 2016). Furthermore, despite the neurobehavioral changes which occur throughout childhood and, in particular, adolescence, relative stability in selected metabolites in all brain region beyond early infancy was observed (Blüml *et al.*, 2013). Another longitudinal MRS study conducted by Holmes *et al.* (2017) evaluated changes in brain metabolites in 64 South African perinatally HIV-exposed children at ages 5, 7 and 9 years. Age-related increases in metabolite levels, such as NAA, Glu and Glu+Gln, across regions of WM and GM were observed and are likely associated with increased myelination and synaptic activity.

A longitudinal analysis was conducted by van Biljon *et al.* (2021) on brain metabolite levels in the same cohort of children, some of whom were participants from the CHER trial, at ages 5, 7 , 9 and 11 years. The study used MRS to evaluate localized brain metabolism to examine and evaluate the long-term consequences of PHIV on brain development in children who have initiated ART at early stages in life and, as a result, have been virally suppressed since a young age. This was performed on the following three brain regions: the BG, mid-frontal gray matter (MFGM) and peritrigonal white matter (PWM). These regions were chosen as they show signs of HIV implication and due to their involvement in healthy brain development (van Biljon *et al.*, 2021). The results of this study showed that PHIV children had significantly elevated tCho across regions as well as elevated Ins in MFGM compared to the uninfected controls. Such findings indicate that, despite early ART initiation, inflammation across the brain in children with HIV persists (van Biljon *et al.*, 2021).

Cross-sectional analyses on the same cohort at each individual age group reported findings both similar and different to these longitudinal studies. At age 5, children with PHIV who initiated ART within 12 weeks were found to have elevated tCho levels in the BG compared to those who had begun treatment later, as well as the uninfected controls (Mbugua *et al.*, 2016). At age 7, no significant metabolic differences were observed between HIV status groups in the BG. However, in the MFGM, decreased Glu and increased tCho concentrations were observed in children with PHIV (Robertson *et al.*, 2018). In the same study by Robertson *et al.* (2018), decreased NAA and Glu levels were found in the BG of PHIV children at age 9. These metabolite changes were not observed at 11 years, yet increased tCho was seen in the MFGM of children with PHIV (Graham *et al.*, 2020).

There have also been studies reporting differences in young adults between 16-25 years of age, an age group generally not investigated. Significantly greater BG tCho/tCr and Ins/tCr were observed in

PHIV young adults compared to the controls (Ashby *et al.*, 2015). The diverse findings at different age groups and studies could be due to demographic and clinical differences in the subjects such as stage of infection and medical history, along with differing MRS acquisition and processing techniques affecting certain factors such as the quality of the data (Robertson *et al.*, 2018; Near *et al.*, 2021; Salan *et al.*, 2023).

There are drawbacks, however, to using the single voxel method as used in the studies previously mentioned. Only one relatively large volume can be selected and examined at a time which requires a *priori* hypotheses to be made about which region to examine. Due to the inhomogeneity of the brain, this region may contain a combination of GM and WM and various structures (Ma *et al.*, 2021). This presents concerns when considering many subjects in which brain size and structures may differ, thus resulting in varying compositions between subjects within the selected voxels. Metabolite concentrations within specific areas may not be accurately represented due to the inclusion of other regions. Furthermore, it requires acquiring ample measurements to account for acquisition-dependent variability associated with MRS measurement (Maudsley *et al.*, 2010). This primarily arises from line-shape distortion, low SNR, variable contributions due to partial volumes from surrounding regions and spectral contamination due to unsuppressed lipid signals and water (Maudsley *et al.*, 2010).

Compared to SVS MRS, MRSI is more affected by factors such as B_1 field inhomogeneity, motion artifacts, imperfect shimming across the scan and frequency drift due to scanner instability (Ma *et al.*, 2021). As a result of this added complexity in processing and analysis, its use is limited to the research community rather than for clinical purposes and studies (Maudsley *et al.*, 2021).

To date, not many studies have investigated the effect of PHIV on individuals using MRSI. MRSI was used by Van Dalen *et al.* (2016) to investigate brain metabolite alterations in children with PHIV at age 12. The method included acquiring and averaging metabolite levels in voxels of segmented GM and WM regions to obtain averaged WM and GM concentrations. Their main observation was elevated tCho/tCr in the WM of children with PHIV compared to the uninfected controls which were associated with poorer cognitive functioning in these children. This finding suggests glial proliferation as a result of ongoing inflammation (Van Dalen *et al.*, 2016). More recently, a study examining metabolic differences in young adults with PHIV between 18-24 years of age using whole-brain MRSI has been published (Salan *et al.*, 2023). The most notable findings were significant elevations in tCho and creatine in PHIV young adults within BG structures such as the caudate, putamen and hippocampus along with both the GM and WM in the brain lobes. These observations suggest increased glial activation resulting in inflammation associated with elevated tCho concentrations and increased

energy metabolism as a result of elevated creatine concentrations (Salan *et al.*, 2023). This is consistent with previous findings of children with PHIV from the CHER trial, but it is of interest to use MRSI techniques to cover a broader region of the brain in the same cohort.

3. Methodology

3.1. Study Participants

The study participants were 165 adolescents of whom 86 were adolescents living with HIV from the CHER trial and 79 were age- and sociodemographically- matched uninfected controls. The uninfected control group comprised 36 children who were born to mothers with HIV (exposed uninfected, HEU) and 43 who were born to uninfected mothers (unexposed uninfected, HUU). All participants received neuroimaging between 14 and 16.5 years as part of an ongoing longitudinal study of brain development in children living with PHIV. All participants living with PHIV had initiated ART before 18 months and were virally suppressed from a young age. At infancy, first-line ART consisted of daily zidovudine and lamivudine with lopinavir-r until 6 months. Thereafter, second-line ART consisted of didanosine, abacavir and nevirapine or efavirenz. At the time of scan, many of the adolescents in this study were on a regime similar to the treatment received at infancy. It consists of combivir (lamivudine and zidovudine), lopinavir-r or abacavir along with new additions, namely efavirenz, atazanavir and TLD (tenofovir, lamivudine and dolutegravir). Of the 86 adolescents with PHIV, 33 were no longer on combivir and lopinavir-r. Table 3.1 shows the demographic data for all participants.

Table 3.0.1: Summary of study demographics

N = 165	**HIV+**	**HEU**	**HUU**
N	86	36	43
Sex (Female, N)	50 (58%)	19 (53%)	22 (51%)
Age at scan (Mean ± SD)	14.9 ± 0.34 yrs	15.2 ± 0.74 yrs	15.1 ± 0.61 yrs

3.2. MRI Data Acquisition

All data was acquired according to protocols approved by the Human Research Ethics Committees of the University of Cape Town and Stellenbosch University. Participants were scanned on a Siemens 3 T Skyra scanner located at the Cape Universities Body Imaging Centre (CUBIC), Groote Schuur Hospital, Cape Town using a 32-channel head coil.

The scanning protocol included a high-resolution T1-weighted structural MRI and volumetric MRSI. The T1-weighted 3D structural MR images were acquired using a multi-echo magnetization-prepared rapid acquisition gradient echo (MEMPRAGE) sequence with the following parameters: 1 mm isotropic resolution; TR = 2530 ms; TE = 1.69, 3.45, 5.39, 7.24 ms; TI = 1100 ms; 176 slices; field of view (FOV) = 224 x 224 mm; flip angle = 7.0°, GRAPPA acceleration factor 2.

MRSI was acquired using spiral-encoded LASER MRSI with the following parameters: FOV = 240 x 240 x 80 mm; TR/TE = 1600/30.0 ms; matrix size = 24 x 24 x 8 (nominal 1 cm^3 voxels), interpolated to 32 x 32 x 8, VOI = 80 x 80 x 40 mm^3, vector size = 512; bandwidth of 1100 Hz; flip angle = 90°, 6 averages, 4 preparation scans, TA = 4min 48s, with water suppression. A water reference measurement was also obtained, omitting water suppression, with identical parameters and only one average.

3.3. Data Processing

The data acquired was processed using a series of steps. The entire processing pipeline is shown in Figure 3.3.

3.3.1. Quality control and spectral processing

The first step involved a visual examination of the spectra for each participant using the preview function in LCModel (Provencher, 2001). The voxel data comprised 32 rows, 32 columns and 8 slices. Subjects who predominantly had spectra with unclear or distorted peaks were identified and excluded. To limit the analysis to voxels within the VOI shown in Figure 3.1 below, we used visual inspection to identify the rows, columns and slices containing good quality spectra. To shorten processing time, we selected spectra within the following range: rows 14 – 19, columns 13 – 20 and slices 3 – 6 for further processing. The selected range of rows and columns is illustrated for a single central slice in Figure 3.2 below.

a) Sagittal b) Coronal c) Axial

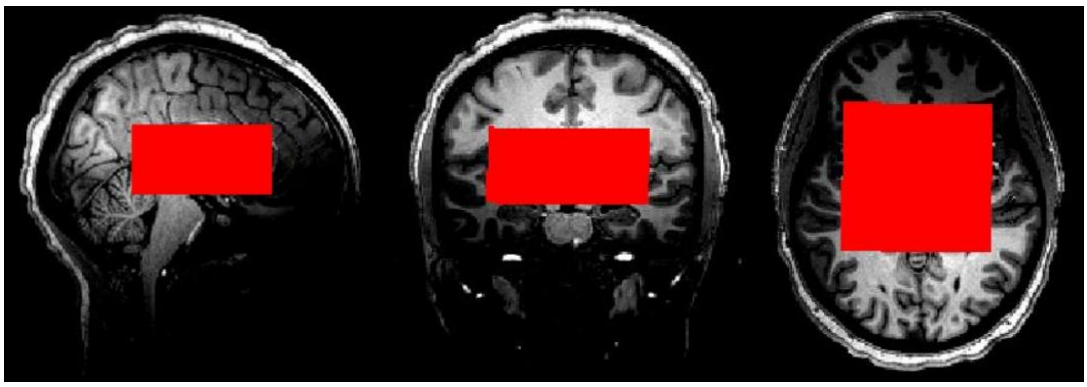

Figure 3.1: Structural MRI showing the positioning of the MRSI VOI within the sagittal, coronal and axial planes.

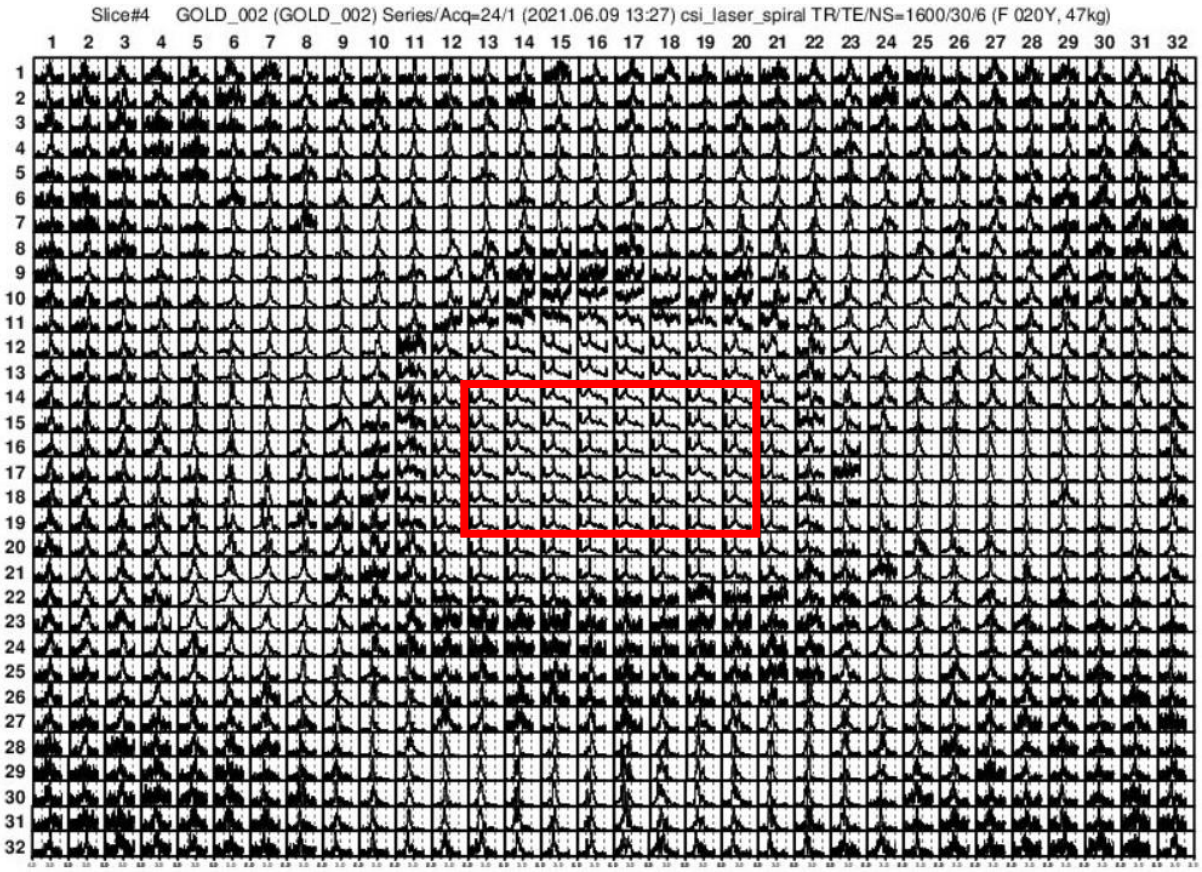

Figure 3.2: Preview of generated spectra and the voxel range selected for further processing using LCModel.

The selected participants' datasets were then processed using a series of scripts and LCModel software (Provencher, 2001) which was used to fit and estimate absolute metabolite concentrations as well as metabolite ratios to creatine. The metabolites of interest included tNAA, GPC, tCr, mI and Glu+Gln. The basis set used for quantification included alanine, ascorbate, aspartate, Cr, GABA, Gln, Glu, glycine, 2-hydroxyglutarate, mI, lactate, PCr, phosphoryl ethanolamine, scyllo-inositol, taurine, NAA, NAAG, PCh, glutathione, glucose and GPC. The acquired spectra were fit to this basis set using a linear combination model fitting algorithm employed by LCModel. This involves each spectrum being modelled as a linear combination of the basis set spectra, each scaled by a corresponding concentration and is well-suited when a short TE, such as 30ms, has been used (Near *et al.*, 2021). Macromolecules and lipids were accounted for through their inclusion as components in the analysis model. After eddy current correction, the signal intensity of the MRSI data was normalized through referencing against unsuppressed water data in LCModel (Stagg *et al.*, 2013; Li *et al.*, 2022). This is to ensure a comparative analysis of metabolite maps between multiple subjects can be done (Maudsley *et al.*, 2021). When generating absolute concentrations using LCModel, the water concentration ($wconc$) was assumed to be constant with a value of 55550 mmol/l with the default attenuation coefficient of 0.7.

The SNR and linewidth expressed as the full width at half maximum (FWHM) given by LCModel were used to further assess spectral quality. SNR is a measure of the strength of the desired signal relative to background noise whereas the FWHM is the width of a peak at half of its maximum height. LCModel used the NAA peak as the linewidth measurement and the SNR and FWHM was generated for each voxel in the obtained MRSI. Based on literature values, we considered spectra with a SNR less than 7 and a FWHM greater than 0.075 for each individual voxel to be of low quality (Mbugua *et al.*, 2016; Holmes *et al.*, 2017). If 20% or more of the voxels for a particular subject did not meet these criteria, the subject was removed from the study.

The structural and MRSI DICOM images for the remaining participants were converted to NIfTI format using the functions dcm2niix (Li *et al.*, 2016) and spec2nii (Clarke *et al.*, 2022), respectively, to be used in subsequent processing steps.

3.3.2. Quantification, mapping, and visualization

The open-source software Oryx-MRSI was used to analyse 3D MRSI data. This software reads in either LCModel outputs or raw spectral data for multiple voxels and generates metabolite maps that are co-registered to the MRSI voxel grid and to the T1-weighted image for each participant (Cengiz *et al.*, 2022, GitHub - sevimcengiz/Oryx-MRSI). This allows for anatomical image segmentation, partial volume correction and registration of metabolite maps to MNI space for intersubject comparison. As it is a MATLAB-based software, adaptations were made using MATLAB 2020a in order to allow us to use it for our data. The different modules included in the software are presented in Figure 3.3 below.

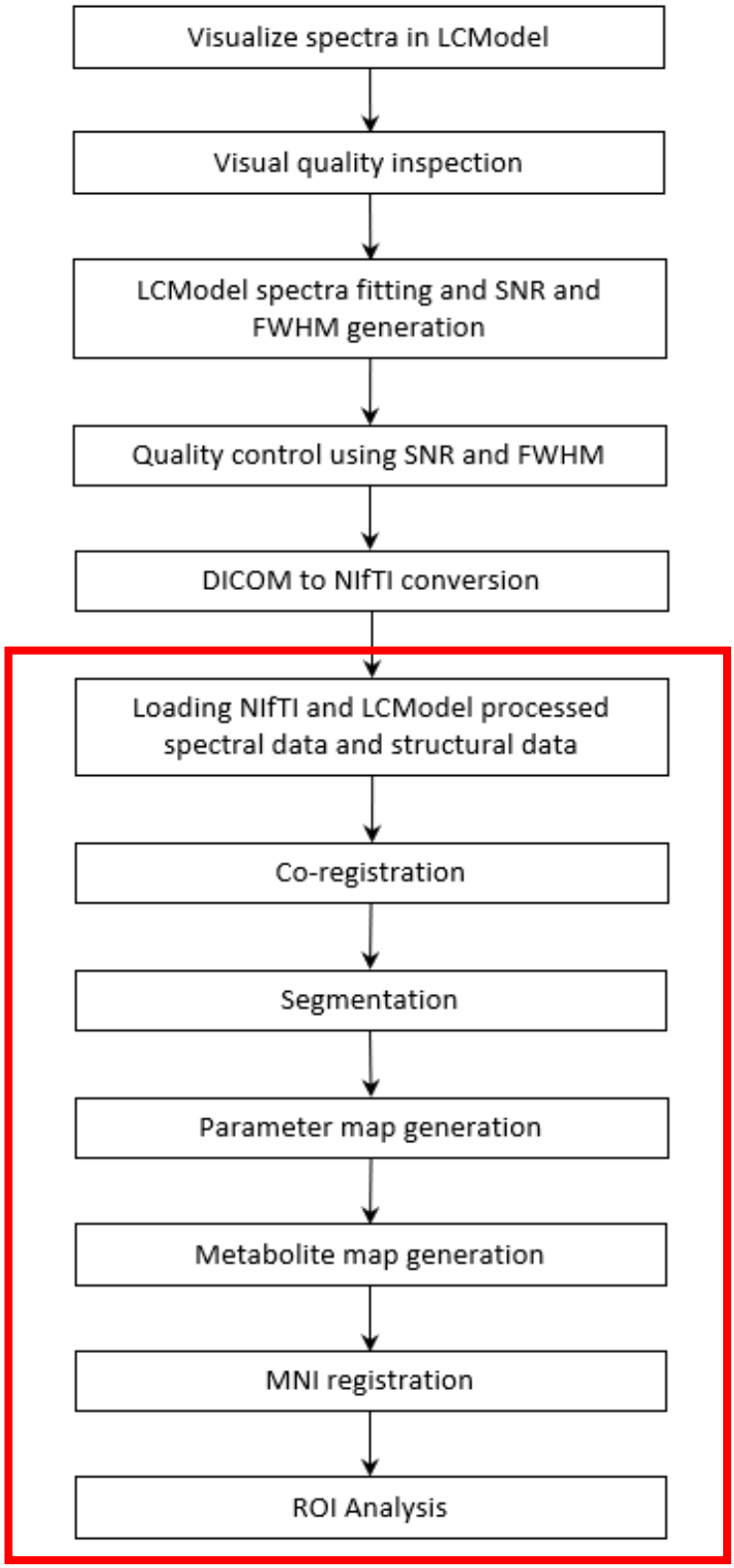

Figure 3.3: Data processing pipeline with the red box indicating the modules included in the Oryx-MRSI software.

Loading Data

The first step involved loading the NIfTI format spectral and structural data for each participant with the nii_tool to be used in subsequent processing steps. The spm_select function from SPM was used to select participants to load and run automatically. For each subject, the LCModel-generated TABLE files of spectral data were loaded and read to extract SNR, FWHM and CRLB parameters, as well as metabolite concentrations for each voxel and store them in individual arrays.

Co-registration

Thereafter, binary masks were created of the FOV (spatially encoded region), VOI (excited volume) and individual MRSI voxels using the co-registration step. This was done by parsing the orientation and position information of scanner-space coordinates from the NIfTI file and using the row, column, and slice for each individual voxel to calculate its size and position (Cengiz *et al.*, 2022).

To create the VOI mask, a matrix representing the coordinates for the eight corners of the VOI was defined after which a rotation and offset from the NIfTI header were applied to calculate these coordinates in the structural image space. Thereafter, a mask was created to match the structural volume dimensions by iterating through all voxels in the structural volume to determine if their distance from the VOI centre fell within the extent of the VOI dimensions. A similar process was followed to create the FOV mask and to generate voxel co-ordinates for each voxel within the region of interest we selected. In this way the spectral data was co-registered to the reference structural image through positioning binary voxel masks onto the same coordinate system at the resolution of the structural image.

Metabolite localization errors, also known as chemical shift displacement (CSD) error, are generally exhibited by localization methods, such as PRESS and STEAM, that are based off of RF/gradient slice selection (Wilson *et al.*, 2019). Therefore, due to larger localization inaccuracies produced by these methods, chemical shift corrections are required to calculate the relative displacement of different metabolites. However, we omitted chemical shift corrections as the scans were done using the LASER localization technique in which the CSD error is greatly reduced compared to that of PRESS (Öz *et al.*, 2023).

Segmentation

After co-registration, the T1w structural volume was segmented into GM, WM and CSF regions using the FMRIB Software Library (FSL). First, FSL's Brain Extraction Tool (BET) was called to remove non-brain tissue from the structural image (Smith, 2002), then the Fast tool was used for segmentation, whilst simultaneously correcting for spatial intensity variations (Zhang, Brady and Smith, 2001). The

fraction of GM, WM and CSF was calculated at each voxel to create maps of fractional CSF (fCSF), GM (fGM) and WM (fWM).

Generation of Quality Control Parameter Maps

The SNR, FWHM and CRLB data from LCModel were used to create multivoxel maps of these parameters for all slices. For array indices outside of the VOI where there was no LCModel output, the SNR and FWHM were assigned default values of 0 and 2 respectively. A spectral quality control step was implemented using cut-off values of > 7 for SNR, < 0.075 ppm for FWHM, < 20% for CRLB and <0.1 for fCSF to exclude voxels within the VOI that did not meet the quality control criteria. A mask was generated for all voxels in the FOV where SNR > 7.

Metabolite Map Generation

Metabolite maps were created using the metabolite concentrations from the LCModel TABLE files positioned onto a 3D MR volume in the same space and resolution as the structural MRI reference image.

This generated absolute concentration maps of tCr, Glu + Gln, GPC, Ins and tNAA, as well as maps of their ratio to tCr. Only GPC was considered and not tCho (GPC + PCh = tCho) as is usually done in MRS studies. This is because in the basis set that was used, PCh was labelled as PCho. As LCModel was programmed to look only for PCh, it was not included and, thus, only GPC concentrations were reported. This is a limitation, however, PCh concentrations were found to be either 0 or negligible at concentration quantified to 10^{-2}, for example 0.002. Furthermore, the average % standard deviation for GPC was low at 9%. Therefore, despite this error, it is believed that the GPC concentration would not be greatly affected with the inclusion of PCh.

To account for partial volume effects due to MRSI voxels containing more than one tissue type, we applied correction to the absolute concentration maps to create tissue-corrected concentration maps as is done by the Osprey software for single voxel MRS data (Oeltzschner *et al.*, 2021). As the ORYX software only applies CSF corrections and thus only generated uncorrected and CSF-corrected concentration maps, a complete correction method, namely the tissue-corrected method, had to be developed and was added to the existing ORYX software code to be applied to the absolute concentrations.

The tissue correction method accounts for differences in both the water concentrations $(wconc)$ and the attenuation of the water signal $(ATTH20)$ due to additional relaxation effects encountered in the different tissue types (GM, WM, and CSF) along with the partial volume effect (Quadrelli, Mountford and Ramadan, 2016). The different water concentrations and attenuation due to relaxation of each

tissue type can be seen in the table below. To account for different voxel tissue compositions, we reversed the original assumed water concentration and attenuation coefficient used in LCModel and used the tissue fraction maps at each voxel to calculate a new voxel-specific water concentration and attenuation factor to use for water scaling.

Table 3.0.2: Parameters used for the Tissue correction method.

Tissue Type	**Variable**	**Water Concentration (mM)** (Gasparovic *et al.*, 2006)	**T_1 (ms)** (Lu *et al.*, 2005)	**T_2 (ms)** (Piechnik *et al.*, 2009)
GM	W_{GM}	43300	1331	110
WM	W_{WM}	35880	832	79.2
CSF	W_{CSF}	55556	3817	503

The attenuation coefficient was calculated, with a TE and TR of 30.0 ms and 1600 ms respectively, using the following equation adapted from (Wansapura *et al.*, 1999; Gasparovic *et al.*, 2006):

$$ATTH20 = exp\left(-\frac{TE}{T_{2W}}\right)[1 - exp\left(-\frac{TR}{T_{1W}}\right)] \quad (1)$$

where TE is the echo time, T_{2W} is the tissue-specific water T_2 relaxation time, TR is the repetition time and T_{1W} is the tissue-specific water T_1 relaxation time. Due to the relatively short TE (30ms) and long TR (> 1.5s) , the metabolite relaxation times were not considered; this avoids challenges associated with using assumed metabolite relaxation times, which may not be accurate (Wilson *et al.*, 2019).

Thereafter, a new relaxation-corrected water concentration $(wconc)$ was calculated inclusive of the weighting associated with different tissue fractions within each voxel. Equation 2 represents the water concentration for GM $(wconc_{GM})$ where W_{GM} is the water concentration for GM equating to 43300 mM, V_{GM} is the GM volume fraction of each voxel calculated in the previous segmentation step, T_{2GM} is 110 ms and T_{1GM} is 1331 ms from Table 3.2. The same was done for WM (equation 3) and CSF (equation 4) using their respective constants from Table 3.2. Thereafter, once all tissue water concentrations were calculated, they were added to obtain an overall water concentration along with correcting for CSF (equation 5). CSF correction accounts for the fact that any part of the voxel that is CSF gives rise to a large water signal, but negligible metabolite signal (Quadrelli, Mountford and Ramadan, 2016; Cengiz *et al.*, 2022). This water concentration was then used to calculate the tissue-corrected concentration after dividing by 55550 x 0.7 to reverse the original assumed water concentration and attenuation coefficient (equation 6).

$$wconc_{GM} = [(W_{GM})(V_{GM})\left(exp\left(-\frac{30}{T_{2GM}}\right)\left(1 - exp\left(-\frac{1600}{T_{1GM}}\right)\right)\right)] \quad (2)$$

$$wconc_{WM} = [(W_{WM})(V_{WM})\left(exp\left(-\frac{30}{T_{2WM}}\right)\left(1 - exp\left(-\frac{1600}{T_{1WM}}\right)\right)\right)] \quad (3)$$

$$wconc_{CSF} = [(W_{CSF})(V_{CSF})\left(exp\left(-\frac{30}{T_{2CSF}}\right)\left(1 - exp\left(-\frac{1600}{T_{1CSF}}\right)\right)\right)] \quad (4)$$

$$wconc = \frac{(wconc_{GM} + wconc_{WM} + wconc_{CSF})}{(1 - V_{CSF})} \quad (5)$$

$$C_{tissue} = \left(\frac{C_0}{55550(0.7)}\right)(wconc) \quad (6)$$

Montreal Neurological Institute (MNI) Registration

The next step involved registering the reference structural MRI onto the Harvard-Oxford subcortical structural brain atlas. This atlas identifies and defines subcortical ROIs, such as the caudate and thalamus, into their left and right structures at a 2 x 2 x 2 mm^3 resolution. To achieve registration, the FSL-FLIRT tool was utilized and, consequently, a transformation matrix was obtained mapping each subject's T1 image to atlas space. This matrix was used to register the spectral images, including the binary masks and all metabolite maps, that were aligned with the structural MRI onto the atlas.

ROI Analysis

The mean, median and standard deviations of the concentration maps within the left and right caudate and thalamus on the MNI structural brain atlas were calculated. The number of voxels in the caudate and thalamus, expressed as a percentage of their total atlas ROI volume, was determined for each metabolite in each participant. This number was slightly different for each metabolite because of the quality control exclusion criteria. All results were then exported to Microsoft Excel spreadsheets.

For statistical analyses, only participants whose voxel grid overlapped with at least 20% of the caudate and thalamus equating to approximately 200 and 520 voxels respectively (at 2 mm^3 resolution) were included. This was done to include as many voxels within the caudate and thalamus as possible to represent the ROI accurately without skewing statistical results. Despite being a low threshold, the 20% overlap was chosen due to the number of subjects that would have to be excluded if a higher threshold were to be used. For example, for the metabolite Ins within the left caudate, approximately 70% of subjects would have to be excluded from the analysis if a threshold of 50% were to be used. This was considered a far too large exclusion. As 20% overlap equates 200 voxels in the caudate and

520 voxels in the thalamus, it is believed that this number of voxels sufficiently represent portions of the caudate and thalamus. Furthermore, to ensure consistency, the 20% overlap was used for all metabolites despite certain metabolites, such as NAA, having greater overlaps than others such as Ins. This can be seen when comparing the mean and min overlap for NAA, which was 81% and 27% respectively, to Ins which was 40% and 1% respectively. Subsequently, despite being a limitation, the 20% overlap was chosen to include as many subjects as possible while sufficiently representing the ROIs.

3.4. Statistical Analysis

Statistical analysis was performed using R statistical software (version 4.3.0) (R Core Team, 2020) for ROI metabolite data and Statistical Parametric Mapping (SPM12) software for voxel-wise comparison of metabolite maps.

3.4.1. Linear Regression Analysis

For each metabolite and each ROI, differences between HIV status groups in tissue-corrected absolute metabolite concentrations and metabolite ratios to tCr were examined using multiple linear regression models in R statistical software while controlling for potential confounding factors such as sex, age at time of scanning (Robertson *et al.*, 2018) and ROI number of voxels. The mean metabolite concentration in the ROI was the dependent variable and the standard deviations of metabolite concentration in the ROI was used as a weighting in these models, such that metabolites with higher standard deviation were weighted lower. The HUU group was used as the reference group so that comparisons were made between HIV+ and HUU subjects as well as between HEU and HUU subjects. As the aim of this study is to specifically examine the effects of HIV exposure on adolescents compared to controls, comparisons between HIV+ and HEU subjects were not included. Outliers in metabolite concentrations were identified as subjects whose metabolite values lay 1.5 times above or below both the upper and lower interquartile range (IQR) respectively (Horn *et al.*, 2001) of the entire group of participants. The models were run first including and then excluding outliers with outliers only being excluded from the final models if there were differences in interpretation between the two approaches. Because the HIV+ group was much larger than the HEU or HUU groups, the analysis was repeated combining the uninfected groups (HEU and HUU) to form an HIV- group which was compared against the HIV+ group. A significance level of $p = 0.05$ was used.

Statistical methods such as linear regression and 3-way ANOVA tests are similar, however, linear regression was chosen as it has greater flexibility and capabilities for handling various predictor types and data situation than ANOVA. It is more suitable when both continuous and categorical predictors, such as age and sex respectively, are present as it allows both to be included in the same model

(Montgomery, Peck and Vining, 2012). The effects of one variable, such as HIV status group, might be affected by another variable, such as sex, and this can be explored using linear regression unlike ANOVA which cannot directly handle such interaction effects. Additionally, the effects of predictors are given a coefficient making it easier to understand the significance of such predictors on the metabolite concentration outcomes, thus, making linear regression the advantageous model for this analysis (Montgomery, Peck and Vining, 2012).

3.4.2. Voxel-wise Analysis

SPM12 was used to perform a voxel-wise analysis of the metabolite maps in MNI space. NAA and GPC were chosen as the metabolites to use for this method of analysis. This was due to the robust nature of these peaks being easily identifiable metabolites as well as having low CRLB values. These characteristics allow for good quality concentration data to be obtained; thus, fewer voxels need to be excluded for quality control. Consequently, there is a greater chance of overlapping voxels when all subjects are aligned and compared in standard space. The remaining metabolites (tCr, Glu+Gln and Ins) were not included in this analysis method as continuous data across all subjects could not be obtained. This is due to the exclusion of many voxels during the quality control steps, resulting in missing voxels or 'gaps' within the MRSI of each subject. As the voxel-wise analysis requires the same voxels in each subject to be overlapped and compared between all subjects, these gaps restricted the number of viable overlaps that could be done. Therefore, insufficient voxel comparisons could be made using the remaining metabolites.

A 2nd-level analysis was done using the factorial design specification module. To look at significant differences between the 3 subject groups, a 3-level analysis of variance (ANOVA) was implemented (Ashburner *et al.*, 2013). The image calculator tool was used to create an explicit mask to ensure all missing voxels within the metabolite maps were assigned a NaN value (Not a Number) across all subjects. The implicit mask feature was enabled to ensure all NaN voxels were excluded from the analysis. SPM contrast manager was used to define different comparisons between the 3 subject groups as seen in the table below.

Table 3.0.3: Summary of group comparisons and their respective contrast weightings used to perform the voxel-wise analysis.

Group Comparisons	**Vector Weighting**
HIV+ > HIV- (HEU + HUU)	[1 -0.5 -0.5]
HIV+ < HIV- (HEU + HUU)	[-1 0.5 0.5]
HIV+ > HUU	[1 0 -1]
HIV+ < HUU	[-1 0 1]

HEU > HUU	[0 1 -1]
HEU < HUU	[0 -1 1]

For each contrast, a *p* value threshold of 0.001 was used and clusters of at least 5 voxels with *p* values below this threshold were extracted. Their locations were then identified in relation to the Harvard-Oxford Subcortical Structural Atlas using the fsl-cluster and atlasquery commands.

Due to the exploratory nature of this analysis method on MRSI data, multiple comparisons were not corrected for. It was unclear whether multiple comparison methods designed for fMRI data would be appropriate for the MRSI data. This is due to the differences in the voxel characteristics between these two modalities. The MRSI voxels obtained are of a larger size (1 cm^3) than fMRI voxels as well as lacking the smoothness that fMRI has. Therefore, this method was used as an initial exploratory analysis within the context of MRSI.

4. Results

The results presented for this study represent cross-sectional analysis of the 3D MRSI data for adolescents at 15 years of age. Firstly, the demographic data of the participants remaining in this study quality control are presented. Thereafter, results from the linear regression analyses on the individual metabolite levels in the left and right caudate and thalamus as well as their ratios to total creatine are presented. Lastly, voxel-wise group comparisons investigating metabolite differences between HIV status groups are summarized.

4.1. Participants remaining after quality control

MRSI data was obtained from 165 adolescents, data from 28 of whom were identified through visual inspection to have noisy or unclear peaks and were, therefore, removed. Using the SNR and FWHM exclusion criteria, along with a threshold of ≤ 20% bad voxels, a further 35 participants were removed. Consequently, a total of 63 participants were removed after both quality control steps, resulting in 102 participants remaining. The demographics of this new sample group are shown in Table 4.1.

Table 4.1: Summary of new sample demographics after quality control steps were performed.

N = 102	**HIV+**	**HEU**	**HUU**	***p***
N	56	19	27	
Sex (Female, N)	36 (72%)	10 (53%)	13 (48%)	0.16
Age at scan (Mean ± SD)	14.8 ± 0.31 yrs	15.1 ± 0.70 yrs	15.0 ± 0.52 yrs	0.23

One-way ANOVA and chi-square test revealed no significant age or sex differences between HIV status groups.

Subjects were further excluded if spectral coverage of the caudate and thalamus region was insufficient (less than 20% equating to 200 and 520 voxels respectively). This varied by region and by metabolite as more subjects fell below the 20% threshold for Ins than for the other metabolites. Therefore, a smaller number of participants' data was included in the analysis for Ins. The number of subjects included in each analysis is summarised for each ROI in Table 4.2. Furthermore, the averaged region overlap % for each HIV status group after considering the 20% exclusion threshold is presented in Table 4.3.

Table 4.2: Sample demographics for each ROI after considering region overlap.

Left & Right Caudate: tNAA, GPC, tCr, Glu+Gln				
N = 94	**HIV+**	**HEU**	**HUU**	***p***
N	51	19	24	
Sex (Female, N)	29 (57%)	10 (53%)	11 (46%)	0.67
Age at scan (Mean ± SD)	15.0 ± 0.41 yrs	15.1 ± 0.70 yrs	15.0 ± 0.50 yrs	0.09
Left Caudate: Ins				
N = 66	**HIV+**	**HEU**	**HUU**	***p***
N	37	14	15	
Sex (Female, N)	23 (62%)	6 (43%)	6 (40%)	0.24
Age at scan (Mean ± SD)	14.9 ± 0.39 yrs	15.0 ± 0.51 yrs	15.0 ± 0.50 yrs	0.04
Right Caudate: Ins				
N = 72	**HIV+**	**HEU**	**HUU**	***p***
N	40	15	17	
Sex (Female, N)	22 (55%)	7 (47%)	7 (41%)	0.61
Age at scan (Mean ± SD)	14.9 ± 0.42 yrs	15.0 ± 0.46 yrs	15.0 ± 0.46 yrs	0.25
Left Thalamus: tNAA, GPC, tCr, Glu+Gln				
N = 79	**HIV+**	**HEU**	**HUU**	***p***
N	46	13	20	
Sex (Female, N)	26 (57%)	6 (46%)	9 (45%)	0.62
Age at scan (Mean ± SD)	14.9 ± 0.42 yrs	14.9 ± 0.45 yrs	14.9 ± 0.45 yrs	0.48
Left Thalamus: Ins				
N = 61	**HIV+**	**HEU**	**HUU**	***p***
N	38	10	13	
Sex (Female, N)	22 (58%)	5 (50%)	7 (54%)	0.89
Age at scan (Mean ± SD)	14.9 ± 0.42 yrs	14.9 ± 0.46 yrs	14.9 ± 0.46 yrs	0.55
Right Thalamus: tNAA, GPC, tCr, Glu+Gln				
N = 84	**HIV+**	**HEU**	**HUU**	***p***
N	50	14	20	
Sex (Female, N)	27 (54%)	9 (64%)	8 (40%)	0.35
Age at scan (Mean ± SD)	14.9 ± 0.44 yrs	14.9 ± 0.44 yrs	14.9 ± 0.44 yrs	0.64
Right Thalamus: Ins				
N = 62	**HIV+**	**HEU**	**HUU**	***p***
N	37	9	16	

Sex (Female, N)	19 (51%)	4 (44%)	8 (50%)	0.93
Age at scan (Mean ± SD)	14.9 ± 0.45 yrs	14.9 ± 0.45 yrs	14.9 ± 0.45 yrs	0.77

Table 4.3: Average % overlap with each ROI for each HIV status group and all metabolites.

			Overlap % (Mean ± SD)		
Region	**Metabolites**	**N**	**PHIV**	**HEU**	**HUU**
Left Caudate	tNAA, GPC, tCr, Glu+Gln	94	84 ± 18	79 ± 22	79 ± 20
	Ins	66	89 ± 12	86 ± 17	88 ± 11
Right Caudate	tNAA, GPC, tCr, Glu+Gln	94	80 ± 20	80 ± 14	82 ± 16
	Ins	72	84 ± 17	86 ± 7	88 ± 12
Left Thalamus	tNAA, GPC, tCr, Glu+Gln	79	48 ± 17	49 ± 15	47 ± 15
	Ins	61	46 ± 17	51 ± 12	45 ± 17
Right Thalamus	tNAA, GPC, tCr, Glu+Gln	84	48 ± 17	44 ± 18	46 ± 14
	Ins	62	54 ± 16	47 ± 18	50 ± 11

4.2. Linear regression on caudate metabolite levels

4.2.1. Left Caudate

The HIV+ group had higher levels of GPC in the left caudate than the HUU controls at 15 years of age (p = 0.02, Table 4.4, Figure 4.1. This finding was also seen when considering the combined uninfected controls (HIV-) (Table 4.5).

No significant differences between the HIV+ and HUU groups were found for other metabolites.

The HEU group had higher levels of tissue-corrected Ins (p = 0.05, Table 4.4) than the HUU group. There were no significant differences between HEU and HUU controls in any of the metabolite ratios to tCr (Table 4.6). However, a trend for reduced GPC/tCr in HEU was observed when analysing metabolite ratios to tCr (p = 0.07, Table 4.6).

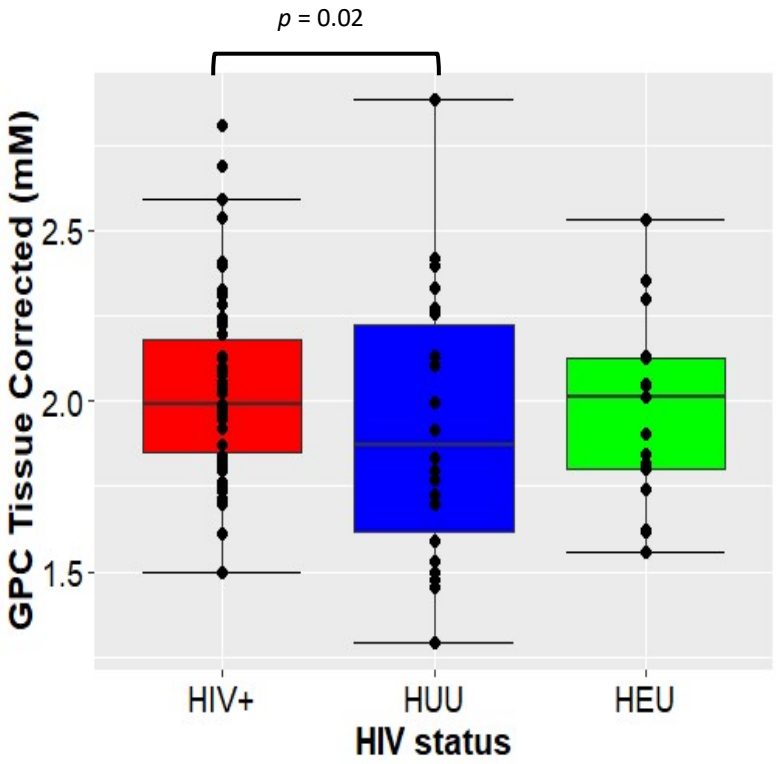

Figure 4.1: Boxplots (with median and IQR) showing the tissue-corrected absolute GPC concentration in the left caudate according to HIV status group.

Table 4.4: Linear regression analysis comparing absolute concentrations of HIV+ and HEU participants to HUU controls in the left caudate. Scanning age, sex and region overlap were controlled for.

	HIV+			HEU		
Metabolite	**B**	**SE**	***p***	**B**	**SE**	***p***
tCr	0.28	0.23	0.22	0.47	0.27	0.09
GPC	0.18	0.07	**0.02**	0.09	0.09	0.30
Glu+Gln	0.29	0.45	0.52	0.07	0.54	0.90
Ins	0.02	0.21	0.93	0.51	0.26	0.05
tNAA	0.59	0.38	**0.04**	0.45	0.46	0.32

B: Unstandardized coefficient, SE: Standard error, *p*: p-value.

Table 4.5: Linear regression analysis comparing absolute metabolite concentrations in the left caudate of HIV+ participants to HIV- (HEU + HUU) controls. Scanning age, sex and region overlap were controlled for.

	HIV+		
Metabolites	**B**	**SE**	***p***
tCr	0.06	0.19	0.75
GPC	0.14	0.06	**0.03**
Glu+Gln	0.26	0.37	0.50
Ins	-0.19	0.18	0.29
tNAA	0.38	0.32	0.24

B: Unstandardized coefficient, SE: Standard error, *p*: p-value.

Table 4.6: Linear regression analysis comparing the ratios of metabolites to tCr of HIV+ and HEU participants to HUU controls in the left caudate. Scanning age, sex and region overlap were controlled for.

	HIV+			HEU		
Metabolites	**B**	**SE**	***p***	**B**	**SE**	***p***
GPC/tCr	-0.00	0.01	0.85	-0.02	0.01	0.07
Glu+Gln/tCr	-0.08	0.05	0.15	-0.11	0.06	0.10
Ins/tCr	-0.01	0.03	0.72	0.02	0.03	0.54
tNAA/tCr	-0.04	0.04	0.28	-0.07	0.05	0.20

B: Unstandardized coefficient, SE: Standard error, *p*: p-value.

Table 4.7: Linear regression analysis comparing the ratios of metabolites to tCr of HIV+ participants to HIV- (HEU + HUU) controls in the left caudate. Scanning age, sex and region overlap were controlled for.

		HIV+	
Metabolites	**B**	**SE**	***p***
GPC/tCr	0.01	0.01	0.32
Glu+Gln/tCr	-0.03	0.04	0.55
Ins/tCr	-0.02	0.02	0.41
tNAA/tCr	-0.19	0.04	0.61

B: Unstandardized coefficient, SE: Standard error, *p*: p-value.

4.2.2. Right Caudate

Within the right caudate, comparisons between the HIV+ and HUU groups yielded no significant differences (Table 4.8) and was further confirmed by the lack of noticeable differences in the metabolites' ratios to tCr (Table 4.9).

Elevated GPC/tCr in the HEU group was observed (p = 0.05, Table 4.9, Figure 4.2). No differences between the HEU and HUU groups were found in the other metabolites.

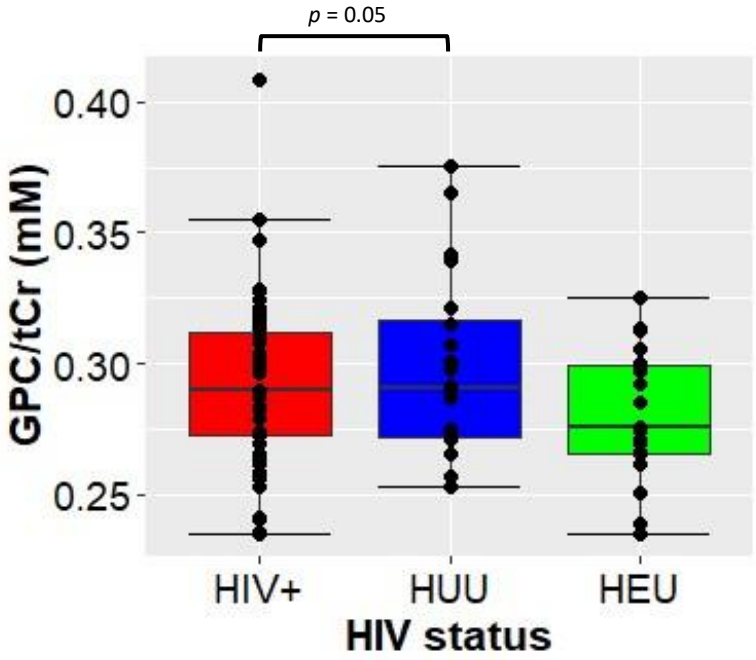

Figure 4.2: Boxplot (with median IQR) showing GPC concentration relative to tCr in the right caudate.

Table 4.8: Linear regression analysis comparing absolute concentrations of HIV+ and HEU participants to HUU controls in the right caudate. Scanning age, sex and region overlap were controlled for.

	HIV+			HEU		
Metabolites	**B**	**SE**	***p***	**B**	**SE**	***p***
tCr	-0.11	0.31	0.74	0.29	0.38	0.45
GPC	-0.01	0.09	0.94	-0.00	0.11	0.94
Glu+Gln	-0.55	0.47	0.25	-0.21	0.56	0.72
Ins	0.23	0.33	0.50	0.14	0.40	0.72
tNAA	-0.00	0.39	1.00	0.32	0.48	0.51

B: Unstandardized coefficient, SE: Standard error, *p*: p-value.

Table 4.9: Linear regression analysis comparing the ratios of metabolites to tCr of HIV+ and HEU participants to HUU controls in the right caudate. Scanning age, sex and region overlap were controlled for.

	HIV+			HEU		
Metabolites	**B**	**SE**	***p***	**B**	**SE**	***p***
GPC/tCr	-0.01	0.01	0.22	-0.02	0.01	**0.05**
Glu+Gln/tCr	-0.03	0.06	0.63	-0.10	0.07	0.18
Ins/tCr	0.03	0.03	0.33	0.03	0.03	0.35
tNAA/tCr	-0.06	0.05	0.25	-0.07	0.06	0.21

B: Unstandardized coefficient, SE: Standard error, *p*: p-value.

4.3. Linear regression on thalamus metabolite levels

4.3.1. Left Thalamus

In the left thalamus, the HIV+ group had higher levels of tissue-corrected Ins (p = 0.04, Table 4.10, Figure 4.3) compared to the HUU controls. Elevated GPC/tCr was additionally seen in the HIV+ group (p = 0.05, Table 4.11).

No significant differences in absolute metabolite concentrations or their ratios to tCr were found between the HEU and HUU groups.

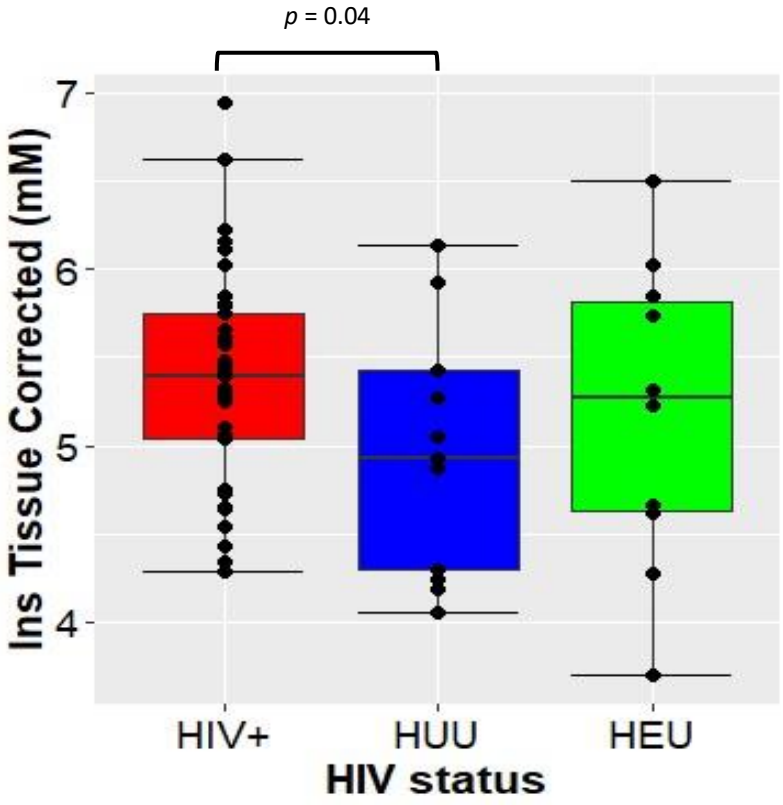

Figure 4.3: Boxplots (with median and IQR) showing the tissue-corrected absolute Ins concentration in the left thalamus according to HIV status group.

Table 4.10: Linear regression analysis comparing left thalamus absolute metabolite concentrations of HIV+ and HEU participants to HUU controls. Scanning age, sex and region overlap were controlled for.

	HIV+			HEU		
Metabolites	**B**	**SE**	***p***	**B**	**SE**	***p***
tCr	0.30	0.22	0.18	0.37	0.31	0.23
GPC	0.06	0.07	0.39	0.03	0.09	0.76
Glu+Gln	0.09	0.39	0.83	0.55	0.54	0.31
Ins	0.44	0.20	**0.04**	0.28	0.28	0.32
tNAA	0.22	0.29	0.45	-0.08	0.39	0.84

B: Unstandardized coefficient, SE: Standard error, *p*: p-value.

Table 4.11: Linear regression analysis comparing the ratios of metabolites to tCr of HIV+ and HEU participants to HUU controls in the left thalamus. Scanning age, sex and region overlap were controlled for.

	HIV+			HEU		
Metabolites	**B**	**SE**	***p***	**B**	**SE**	***p***
GPC/tCr	0.02	0.01	**0.05**	0.00	0.01	0.92
Glu+Gln/tCr	-0.07	0.04	0.09	0.04	0.06	0.50
Ins/tCr	-0.01	0.03	0.81	-0.04	0.04	0.29
tNAA/tCr	-0.04	0.04	0.39	-0.07	0.06	0.23

B: Unstandardized coefficient, SE: Standard error, *p*: p-value.

4.3.2. Right Thalamus

Similarly to the left thalamus, the tissue-corrected Ins concentrations were elevated in the HIV+ group (p = 0.03, Table 4.12, Figure 4.4).

Increased tissue-corrected Ins concentrations were also present in the HEU group compared to the HUU controls (p = 0.01, Table 4.12, Figure 4.4). This finding was complemented by higher Ins/tCr levels (p = 0.02, Table 4.13).

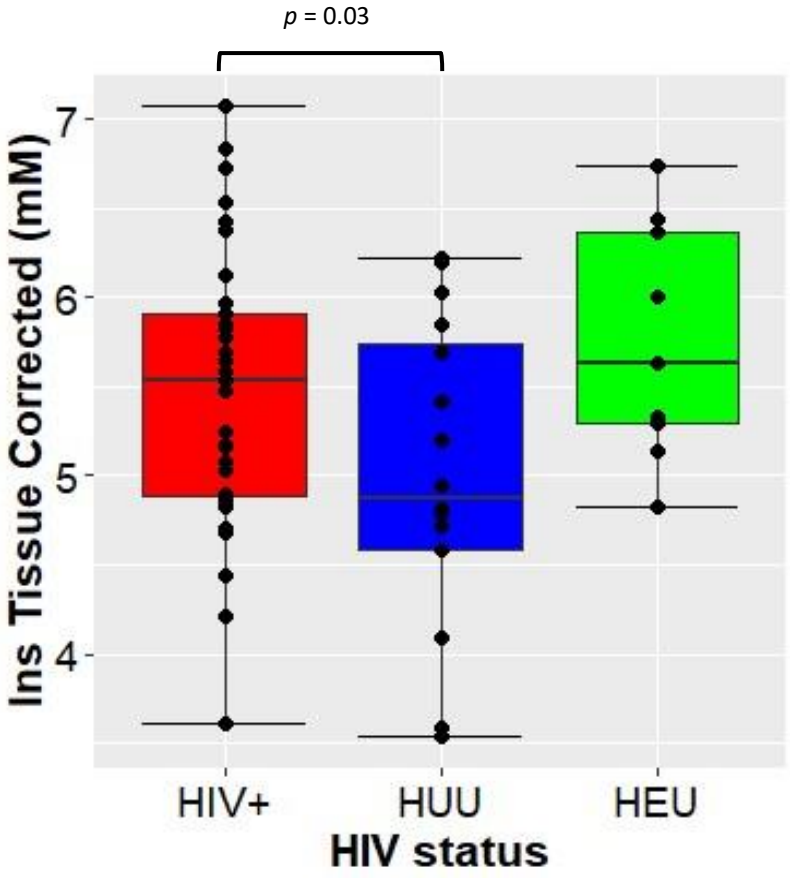

Figure 4.4: Boxplots (with median and IQR) showing the tissue-corrected absolute Ins concentration in the right thalamus according to HIV status group.

Table 4.12: Linear regression analysis comparing absolute concentrations of HIV+ and HEU participants to HUU controls in the right thalamus. Scanning age, sex and region overlap were controlled for.

	HIV+			HEU		
Metabolites	**B**	**SE**	***p***	**B**	**SE**	***p***
tCr	0.06	0.24	0.80	0.00	0.32	0.99
GPC	0.07	0.04	0.09	0.04	0.05	0.42
Glu+Gln	-0.19	0.39	0.63	0.75	0.53	0.17
Ins	0.45	0.21	**0.03**	0.75	0.29	**0.01**
tNAA	-0.06	0.32	0.85	-0.24	0.43	0.57

B: Unstandardized coefficient, SE: Standard error, *p*: p-value.

Table 4.13: Linear regression analysis comparing the ratios of metabolites to tCr of HIV+ and HEU participants to HUU controls in the right thalamus. Scanning age, sex and region overlap were controlled for.

	HIV+			HEU		
Metabolites	**B**	**SE**	***p***	**B**	**SE**	***p***
GPC/tCr	0.00	0.01	0.70	-0.01	0.01	0.48
Glu+Gln/tCr	-0.02	0.05	0.70	-0.02	0.06	0.81
Ins/tCr	0.05	0.03	0.10	0.09	0.04	**0.02**
tNAA/tCr	-0.03	0.03	0.40	-0.03	0.04	0.44

B: Unstandardized coefficient, SE: Standard error, *p*: p-value.

4.4. Voxel-wise analysis

4.4.1. Analysis of GPC absolute concentrations

Voxel-wise analysis was performed on GPC metabolite concentration maps and was repeated for each contrast listed in Table 3.3. Table 4.14 and Table 4.15 present results for the HIV+ > HIV- and HIV+ >HUU contrasts that produced clusters larger than 5 voxels.

There were several fairly large clusters where HIV+ adolescents had higher GPC concentration than controls. The largest clusters were found in the right and left thalamus (Table 4.14) and can be seen in the axial slice at Y = 6 in Figure 4.5. There were also clusters of elevated GPC in the left putamen and right pallidum.

Table 4.14: Voxel clusters identified through the voxel-wise analysis of tissue-corrected GPC absolute concentrations and HIV+ > HIV- contrast.

Cluster Index	Predominant Region Overlap	Number of Voxels	Max T	COG X	COG Y	COG Z
17	Right Thalamus	45	4.17	38.4	57.3	38.4
16	Left Thalamus	44	4.29	50.1	56.8	39.2
15	Left Lateral Ventricle	30	3.85	46.9	56.8	45.6
14	Left Putamen	24	4.07	59.7	59.7	36.9
13	Right Pallidum	23	4.49	33.5	59.7	36.1
12	Left Cerebral White Matter	7	3.98	59.9	53.4	33.1
11	Right Putamen	5	3.78	30.8	55.4	35
10	Left Caudate	5	4.09	52.1	69	37.4

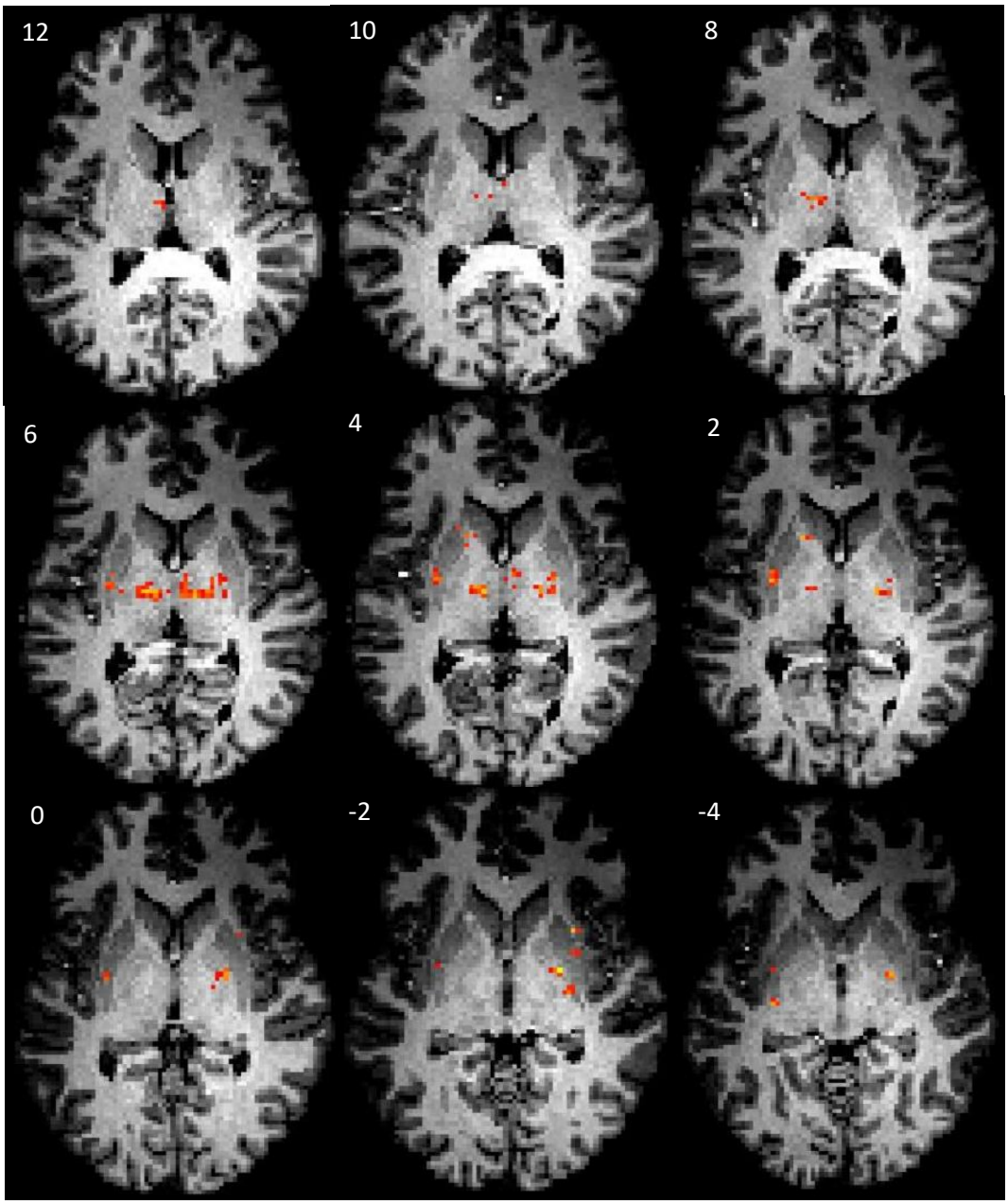

Figure 4.5: SPM maps of axial slices rendered on to a MNI-registered T1-weighted structural image showing areas of significantly higher tissue-corrected GPC concentration in adolescents with PHIV compared to the uninfected controls (thresholded at uncorrected $p < 0.001$ and the extent of 5 voxels).

When comparing the HIV+ group to the HUU controls only (HIV+ > HUU), the largest clusters identified were in the right putamen and left caudate (Table 4.15). These clusters can be seen in the axial slices corresponding to Y = -2 and Y = 6 respectively in Figure 4.6.

Table 4.15: Voxel clusters identified through the voxel-wise analysis of the tissue-corrected GPC absolute concentrations and HIV+ > HUU contrast.

Cluster Index	Predominant Region Overlap	Number of Voxels	Max T	COG X	COG Y	COG Z
22	Right Putamen	35	4.78	29.7	65	35
21	Left Caudate	20	4.31	51.8	68.8	38
20	Left Thalamus	13	3.92	47.4	57.1	42.5
19	Left Putamen	12	4.25	59.4	59.8	36.7
18	Right Cerebral White Matter	8	4.07	33.2	71.4	41.6
17	Right Cerebral White Matter	6	3.53	32.3	67.7	41.7
16	Right Thalamus	5	3.41	42.8	59.4	41

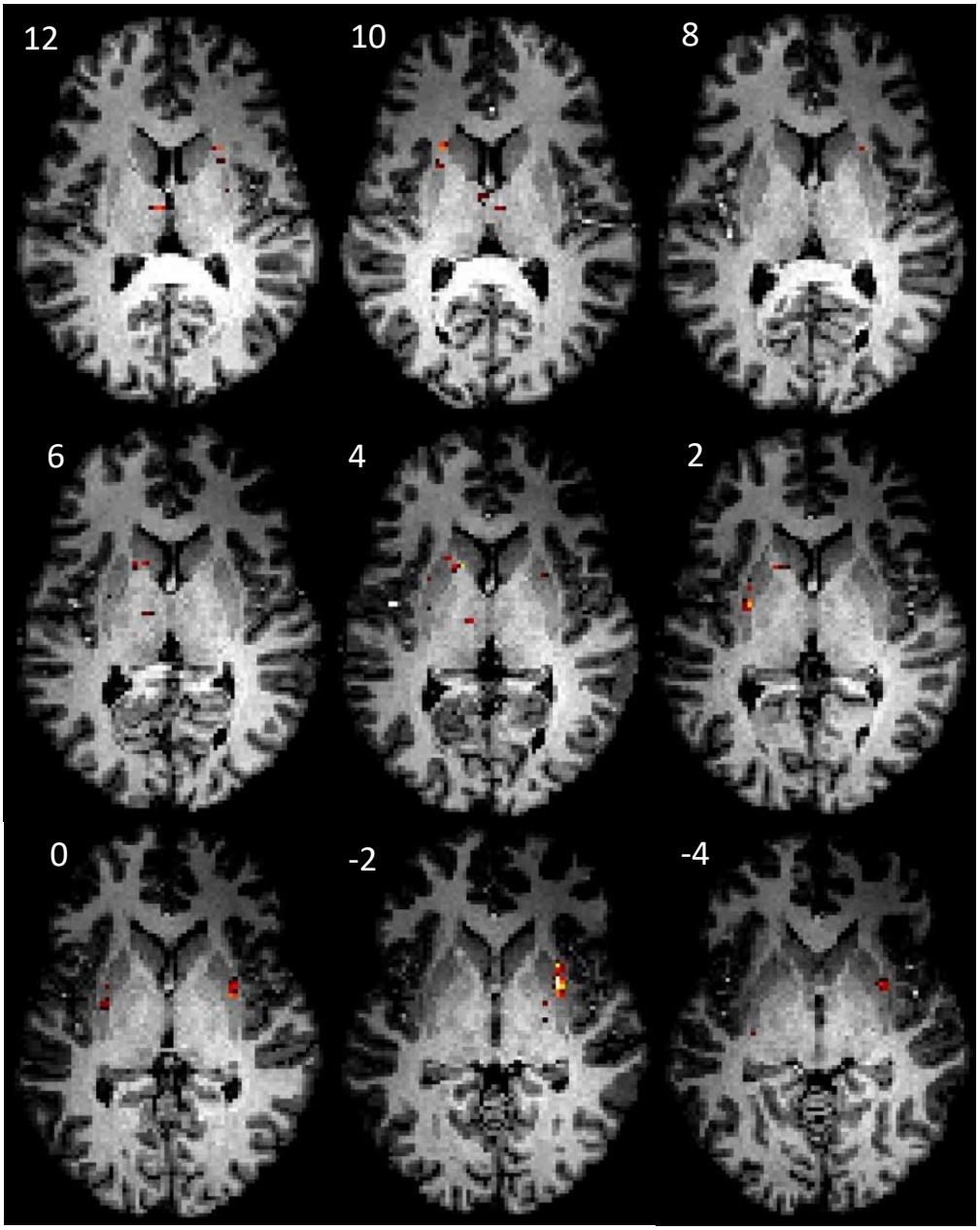

Figure 4.6: SPM maps of axial slices rendered on to a MNI-registered T1-weighted structural image showing areas of significantly higher tissue-corrected GPC concentration in adolescents with PHIV compared to the HUU group (thresholded at uncorrected $p < 0.001$ and the extent of 5 voxels).

4.4.2. Analysis of NAA absolute concentrations

The tissue-corrected NAA concentration voxel-wise analysis results are presented in Table 4.16 and 4.17. There was a reasonably large cluster (32 voxels) in the left thalamus where HIV+ adolescents had higher tissue-corrected NAA concentrations than HIV- adolescents (HIV+ > HIV-, Table 4.16, Figure 4.7). When compared only to unexposed controls (HUU), HIV+ adolescents had clusters of higher NAA overlapping the right (21 voxels) and left (9 voxels) putamen, but none of the significant clusters identified were located in our *a priori* regions of interest (Table 4.17, Figure 4.8).

Table 4.16: Voxel clusters identified through the voxel-wise analysis using the tissue-corrected NAA absolute concentrations and HIV+ > HIV- contrast.

Cluster Index	Predominant Region Overlap	Number of Voxels	Max T	COG X	COG Y	COG Z
6	**Left Thalamus**	**32**	**4.41**	**51.2**	**57.4**	**38.9**
5	Right Thalamus	7	3.57	41.7	56.0	38.6
4	Right Pallidum	5	4.02	33.4	59.4	38.2

a) Sagittal b) Coronal c) Axial

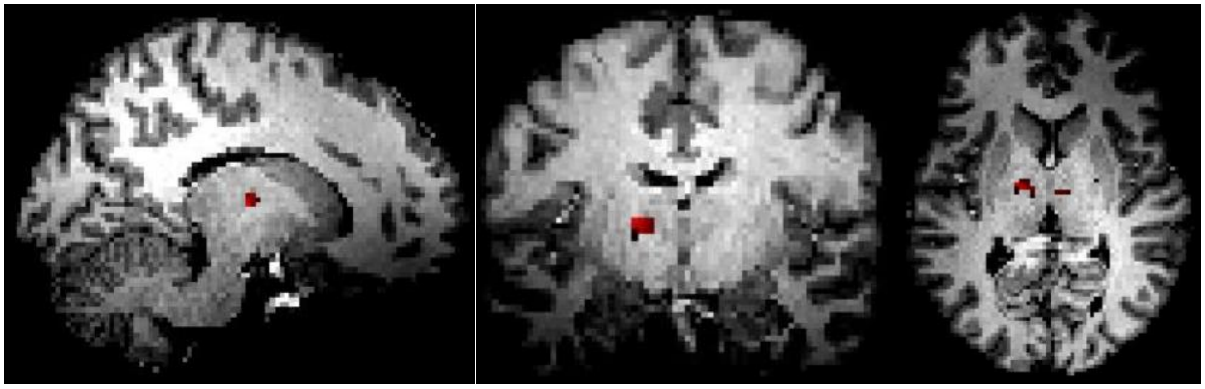

Figure 4.7: SPM sagittal, coronal and axial maps rendered on to a MNI-registered T1-weighted structural image showing 3 clusters of significantly higher tissue-corrected NAA concentration in adolescents with PHIV compared to the uninfected controls (thresholded at uncorrected $p < 0.001$ and the extent of 5 voxels).

Table 4.17: Voxel clusters identified through the voxel-wise analysis of tissue-corrected NAA absolute concentrations and HIV+ > HUU contrast.

Cluster Index	Predominant Region Overlap	Number of Voxels	Max T	COG X	COG Y	COG Z
10	Right Putamen	21	4.29	29.6	64.9	35.4
9	Left Putamen	9	4.08	58.8	66.9	37.5
8	Right Cerebral White Matter	6	4.28	30.8	61.9	42.6

a) Sagittal b) Coronal c) Axial

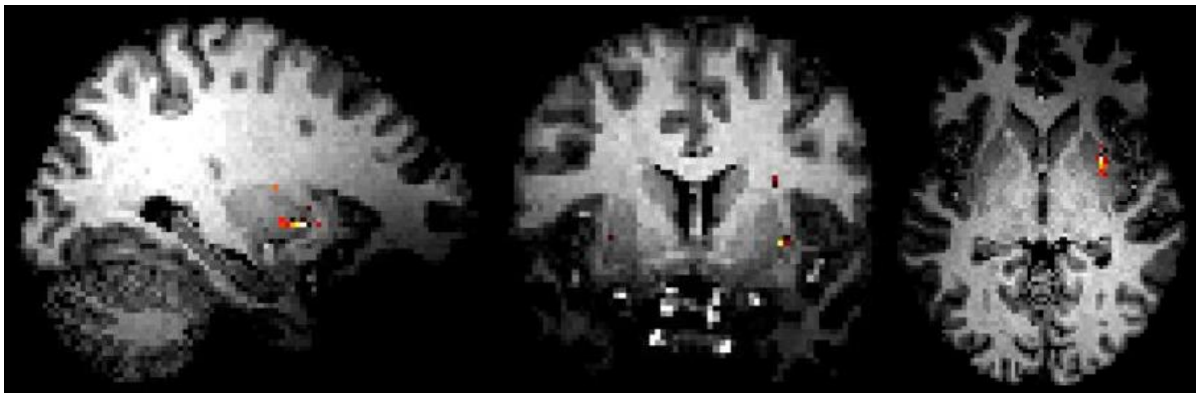

Figure 4.8: SPM sagittal, coronal and axial maps rendered on to a MNI-registered T1-weighted structural image showing 3 clusters of significantly higher tissue-corrected NAA concentration in adolescents with PHIV compared to the HUU group (thresholded at uncorrected $p < 0.001$ and the extent of 5 voxels).

5. Discussion

This study investigated the metabolite levels within the caudate and thalamus of adolescents with PHIV, who are on ART, compared to adolescents without HIV at approximately 15 years of age. In addition to investigating whether there are differing metabolic profiles between the different HIV status groups, we also aimed to create metabolite maps in standard space at interpolated resolution and to compare different MRSI analysis approaches namely an atlas-based region of interest (ROI) analysis and voxel-wise comparison. Both aims aspired to gain understanding of whether HIV and prolonged ART exposure result in any neurometabolic changes in adolescents, an age demographic that has been sparsely studied (Mofenson and Cotton, 2013). Furthermore, there was the hope to establish a MRSI approach using an atlas-based metabolic quantification pipeline that offered a complete unbiased characterization of specific regions of interest that could be used for future spectroscopic studies.

Using multiple linear regression models, we identified metabolic changes within the selected regions, namely the caudate and thalamus, in adolescents with PHIV compared to uninfected HUU controls. We then used a voxel-wise between group comparison in which voxel clusters representing metabolic differences between HIV status groups were identified. Our main findings include increased GPC, referred to as glycerophosphocholine, in the caudate, and Ins in the thalamus in adolescents with PHIV relative to uninfected controls. The elevated levels of both these metabolites together, although in different regions, point to ongoing inflammation in adolescents with PHIV despite early ART commencement.

5.1. Effects of PHIV on metabolite levels

5.1.1. Elevated glycerophosphocholine in the caudate ROI in PHIV

Within the left caudate, elevated levels of glycerophosphocholine for the PHIV group compared to the HUU controls were observed. This finding was lateralized to the left hemisphere of the brain, as the right caudate did not present any glycerophosphocholine metabolic alterations. Higher levels of glycerophosphocholine in the PHIV group were still seen compared to a combined HIV- group consisting of all uninfected adolescents, both HUU and HEU.

Choline within the brain is generally considered a biomarker of cellular synthesis, degradation and injury as choline is essential for the structural integrity of neuronal and glial phospholipids due to its role in the synthesis of phosphatidylcholine, a key membrane constituent. Choline is a marker of glial proliferation with glial cells being an important regulator of the neuronal environment (Hansson and Ronnback, 2003). In individuals with HIV, inflammatory compounds such as cytokines and chemokines

are released through glial cells such as infected microglia and macrophages and present more robust associations with cognitive performance than markers representing disease severity (Gonzalez-Scarano and Martin-Garcia, 2005). These compounds then cause nearby microglia and other cell types, for example, astrocytes, to be activated and release additional toxic compounds, thus perpetuating the cycle of neuroinflammation (Zahr *et al.*, 2014; Gamage *et al.*, 2020). Additionally, astrocytes can shift from a protective "neuronal focused" role to one focusing on inflammation due to inflammatory stimuli received from the microenvironment. Therefore, elevated choline is observed in inflammatory conditions and is often associated with activated microglia and astrocytes caused by pro-inflammatory cytokines (Chang *et al.*, 2013; Gamage *et al.*, 2020). Furthermore, Van Dalen *et al* (2016) reported poorer cognitive performance in children with HIV when elevated choline levels were observed, suggesting an association between increased glial activation and poorer cognitive functioning.

Choline also affects the degree of axonal integrity through the synthesis of myelin sheath-associated compounds such as sphingomyelin and is a precursor to acetylcholine, a neurotransmitter involved in motor, sensory and cognitive functions (Govindaraju, Young and Maudsley, 2000; Zeisel, 2006; Li *et al.*, 2017). Choline also plays a role as a cerebral osmolyte with the cholinergic system aiding in neural modulation (Govindaraju, Young and Maudsley, 2000; Li *et al.*, 2017). Therefore, the elevated glycerophosphocholine levels observed in the PHIV group suggests a breakdown of these compounds. This leads to cell membrane degradation, demyelination, microglial proliferation and reactive astrogliosis (Van Dalen *et al.*, 2016; Salan *et al.*, 2023) and reflects potential inflammation within the left caudate (Mbugua *et al.*, 2016; Salan *et al.*, 2023). Studies observing age-related changes in healthy individuals from birth to adolescence have reported choline concentration to decline and reach a plateau at approximately 5 years of age continuing into adolescence within deep grey nuclei sites consisting of the caudate, putamen and thalamus (Blüml *et al.*, 2013). This suggests that the increased glycerophosphocholine we observed within the left caudate is not a feature of typical adolescent brain development.

Our results are consistent with the previous findings from the parent longitudinal study on the same cohort of children. A prior analysis at 5 years of age detected higher levels of choline within the BG in PHIV children from the CHER trial who had initiated ART within 12 weeks of age compared to those who began treatment after this period as well as compared to the uninfected children (Mbugua *et al.*, 2016). Increased volumes of BG structures including the left and right nucleus accumbens and putamen as well as the left globus pallidus were also observed in the children with PHIV compared to the controls (Randall *et al.*, 2017). It was hypothesized that the increased volume of these structures is due to inflammation caused by leukocyte infiltration and reactive gliosis. Both findings by Mbugua

et al. (2016) and Randall *et al.* (2017) together suggest an associated between increased choline and increased cell proliferation and influx in the BG in children with PHIV at 5 years of age.

In contrast, no significant difference in BG choline concentration was reported in a metabolic analysis of children with PHIV and controls at 7 and 9 years (Robertson *et al.*, 2018). In a parallel structural analysis at 7 years, reduction in BG volumes such as the right putamen was observed in children with PHIV (Nwosu *et al.*, 2019). Therefore, the lack of elevated choline concentration in the BG along with the decrease in right putamen in children with PHIV could suggest that by 7 years of age, there is a reduction in the initial inflammatory response within the BG previously observed at 5 years. Furthermore, choline levels between children with PHIV and HUU children were found to be similar at age 11 (Graham *et al.*, 2020) and so these findings indicate the stabilization of choline concentrations between ages 7 and 11.

van Biljon *et al.* (2021) used a longitudinal approach to examine HIV-related metabolite trajectories in children from the CHER trial between 5 and 11 years. Significantly elevated choline levels were observed across several regions, including the BG, in children with PHIV compared to the uninfected controls. This is contrary to the reports of no alterations in choline concentration with PHIV at age 7, 9 or 11 (Robertson *et al.*, 2018; Graham *et al.*, 2020). However, the longitudinal nature of this study affords additional power to detect elevated choline findings across brain regions including the BG (van Biljon *et al.*, 2021) compared to the cross-sectional analysis at ages 7, 9 and 11 years of age (Robertson *et al.*, 2018; Graham *et al.*, 2020). Additionally, elevated BG choline was apparent in both the absolute and ratio to tCr data for children with PHIV and can be, therefore considered a robust result.

However, despite finding elevated glycerophosphocholine in the tissue-corrected data, we did not see elevated glycerophosphocholine/tCr. Cr is commonly used as a reference metabolite as its spectral peak is well defined and thought to be relatively stable and consistent across different brain regions when compared to the other primary metabolites (NAA and choline) (Govindaraju, Young and Maudsley, 2000; Cecil, 2013). When using ratios, it is expected that experimental conditions such as field inhomogeneities, acquisition parameters and partial volume contaminations from CSF, which is assumed to be free of metabolites, are the same for both metabolites used in the ratio and, therefore, they do not need to be corrected for (Li, Wang and Gonen, 2003). Despite these advantages in using Cr as a secondary reference, the stability of Cr may be questioned due to factors such as possible age-related changes. This can lead to inaccuracies in the metabolite ratios, therefore, the results from the water referenced absolute concentrations should be given most weight. A reason for unchanged glycerophosphocholine/tCr could be due to Cr also changing along with glycerophosphocholine, thus,

negating any ratio changes. However, this is not thought to be the case as no changes in absolute Cr concentrations were observed.

Studies on other cohorts have reported similar findings to ours. In a recent whole-brain cross-sectional MRSI study on young adults with PHIV between the ages 18 and 24, the most notable metabolic alterations were observed in choline, with significantly increased concentrations in multiple brain regions (Salan *et al.*, 2023). These included BG structures such as the caudate and putamen, as well as the hippocampus. Greater choline/tCr ratios were also seen in the BG in a cohort of young adults with PHIV compared to uninfected controls within the age range of 16 and 25 years (Ashby *et al.*, 2015). These findings, along with those observed in this study, collectively suggest continued elevated choline concentrations throughout adolescence and young adulthood. As a result, we can postulate that this in indicative of ongoing inflammation reflective of continuing activation of the immune system within the CNS (Ashby *et al.*, 2015). Approximately 80% of the adolescents with PHIV from these studies were on ART, however, less than half were found to be virally supressed (Ashby *et al.*, 2015; Salan *et al.*, 2023). This could indicate poor ART adherence among them and potentially be the cause of the elevated choline observed in these PHIV groups.

Not only have these regions exhibited metabolic differences in adolescents with PHIV, but functional and structural differences have also been observed. Functional MRI (fMRI) studies investigating the effects of PHIV on adolescents have reported hypoactivation of the left caudate, a structure generally associated with executive functioning, in adolescents with PHIV compared to the uninfected control group (Melrose *et al.*, 2008). The PHIV cohort also exhibited executive deficiencies in self-regulation and inhibition and mental flexibility. Evidence has shown the route of HIV infection directly affects subcortical structures due to their close proximity to the lateral ventricles (Thompson *et al.*, 2006); therefore, it is postulated that these results may be due to white matter tract deficits which link the caudate to frontal cortices (Melrose *et al.*, 2008). As the caudate is tightly linked to emotional stimuli and reward reactivity and processing, its role in facilitating goal directed behaviour is of great importance particularly during the period of adolescence (Dumontheil, 2016). Cognitive functioning has also been associated with differences in metabolite concentrations with increased choline/tCr in the GM of adolescents with PHIV being related to poorer executive functioning, memory and attention. Associations between glial markers and cognition were observed in PHIV cohort which suggests glial proliferation induced by HIV may have a negative impact on cognitive functioning (Van Dalen *et al.*, 2016).

Evaluations of subcortical grey matter deformation in adolescents with PHIV at 16 years of age identified clusters in which higher peak viral load had increased inward deformation in the caudate,

thalamus, putamen and globus pallidus with local inward deformation being associated with smaller volumes of whole subcortical structures. Furthermore, those with inward deformation in the caudate and thalamus performed worse cognitively in many domains (Lewis-de los Angeles *et al.*, 2016) as these structures are involved in higher-order cognitive functioning (Giedd *et al.*, 2006). These findings were observed despite the adolescents being on cART which suggests persistent HIV during periods of critical and rapid brain development (Lewis-de los Angeles *et al.*, 2016).

The regional analysis of the caudate through a combination of metabolic, functional and structural modalities can provide a more robust and confirmative conclusion that PHIV does affect such ROIs in adolescence and should, therefore, be investigated further as a multi-modal study.

5.1.2. Elevated tNAA in the caudate ROI in PHIV

Along with elevated glycerophosphocholine levels, significant increases in tNAA concentrations were also detected in the left caudate in adolescents with PHIV compared to the controls. At 5 years of age, children receiving early ART were found to have higher levels of absolute NAA concentrations than the uninfected controls (Mbugua *et al.*, 2016) as was seen similarly by Keller *et al.* (2004). This was further confirmed by the elevated NAA levels in the BG observed by van Biljon *et al.* (2021) again at 5 years.

No NAA differences were found in a subset of adolescents with PHIV from this study and controls at 7 years. Additionally, these children were found to have decreased BG NAA at 9 years, suggesting neuronal damage (Harezlak *et al.*, 2011; Robertson *et al.*, 2018). This indicates that HIV has an effect on the metabolite trajectory of NAA in that it does not follow the normal increase associated with age (Robertson *et al.*, 2018). According to studies looking at the metabolic maturation of healthy brains from birth through to adolescence, NAA is reported to increase between the ages of 5 and 12 followed by a plateau during adolescence in subcortical gray matter sites such as the caudate and thalamus (Blüml *et al.*, 2013). As NAA is normally interpreted as a marker of axons representing neuronal integrity (Blüml *et al.*, 2013), elevated BG NAA in adolescents with PHIV is unexpected.

However, contrary to these observations, the age-related trajectory for NAA showed, despite the elevated NAA seen at 5 years, a slower increase in concentration with age between 5 and 11 years in PHIV relative to controls, reaching a comparable level to uninfected controls at age 11 (van Biljon *et al.*, 2021). This was supported by (Graham *et al.*, 2020) in which no BG NAA differences between HIV status groups were observed at age 11. Therefore, following this trend, we postulated that there would be reduced NAA levels compared to the HUU group as these children with PHIV reached adolescence, however, this was not observed at 15 years. These observations imply that despite the

inferred inflammation in the BG, the neuronal integrity within this region may not be significantly disrupted in adolescents with PHIV and young adults at this stage of their lives (Ashby *et al.*, 2015).

Age-related increases in BG tNAA concentrations in HIV- controls from this cohort were also reported between 5 and 9 years (Holmes *et al.*, 2017). This was found in conjunction with increasing Glu levels, which was thought to lead to increased NAAG production contributing to the increased tNAA levels seen. Increased BG NAAG could be due to its role in regulating the release of glutamate and dopamine (Moffett *et al.*, 2007). Due to the increased demand of such during childhood and into adolescence, increased NAAG production could occur to moderate neurotransmitters (Holmes *et al.*, 2017).

5.1.3. Elevated Ins and glycerophosphocholine/tCr in the thalamus ROI in PHIV

At the age of 15 years, we detected elevated levels of Ins within the thalamus bilaterally in adolescents with PHIV compared to the HUU controls. Ins is a vital messenger involved in the transduction of cellular signals and is predominantly utilized as a glial marker (Govindaraju, Young and Maudsley, 2000; Ashby *et al.*, 2015; Van Dalen *et al.*, 2016; Li *et al.*, 2022). Altered levels in Ins concentrations are associated with brain injury and Alzheimer's disease (Govindaraju, Young and Maudsley, 2000).

Furthermore, Ins plays a key role in the regulation of cell volume, therefore, increased Ins may suggest cell shrinkage and chronic inflammation as a result of increased gliosis (Harezlak *et al.*, 2011; Ashby *et al.*, 2015; Van Dalen *et al.*, 2016). However, Ins is not only limited to glial cells but also observed in neuronal cell lines (Novak *et al.*, 1999) which could be a possible reason for the unaltered Ins levels seen in previous studies of PHIV children ages 7 and 9 years (Robertson *et al.*, 2018) and 11 to 15 years (Van Dalen *et al.*, 2016). Additionally, unaltered choline and Ins were reported in PHIV children between ages 5 and 11 years with levels temporarily dropping at 5 years below that of an adult (Kries, Ernst and Ross, 1993). This contrasts the findings by van Biljon *et al.* (2021) where elevated BG Ins was observed in the longitudinal analyses on PHIV children between this same age range. However, the region in which this was observed consisted mainly the caudate whereas our elevated Ins findings were in the thalamus. Despite these differing regions, inflammation in the thalamus can be deduced due to the link established between elevated Ins and inflammation.

We also observed increased glycerophosphocholine/tCr ratios in the left thalamus only. Elevated choline and Ins are regarded as early markers of inflammation that precede neurological injury, usually signalled by decreases in NAA concentrations or damage visible on MRI (van Biljon *et al.*, 2021). Increased choline concentration alone is reportedly not strong enough indication to conclude inflammation in a region. This is because during inflammation, elevated Ins along with choline is expected (Harezlak *et al.*, 2011). Therefore, our findings of increased glycerophosphocholine and Ins concentrations, both of which are inflammatory metabolite factors (Chang *et al.*, 2003; Ashby *et al.*,

2015), signify ongoing inflammation and possible astrocytosis in adolescents with PHIV despite early treatment.

5.1.4. Voxel-wise comparison between adolescents with PHIV and controls

Voxel-wise analyses in MRI are typically used for investigating structural aspects and functional connections and networks in the brain. As a result, spectroscopic studies using the voxel-wise method as a tool for analysis are not commonly seen. However, measuring metabolite distribution without specifically defined ROIs will allow for unbiased investigation across the whole brain and is an important consideration during analysis (Young *et al.*, 2010). A voxel-wise two-group ANOVA analysis was performed on MRSI data to assess whole-brain topography of multiple-sclerosis associated metabolic disorders (Donadieu *et al.*, 2016). To our knowledge, no previous voxel-wise metabolic analysis using MRSI- derived data has been done to investigate the effects of PHIV on individuals.

An ANOVA statistical test was chosen to perform between group analyses as was done by Donadieu *et al.* (2016). Furthermore, the use of brain masks to exclude specific voxels were also used. However, we used fsl-cluster and atlasquery functions to label significant clusters as opposed to the SPM8 function WFU PickAtlas toolkit used by Donadieu *et al.* (2016).

We chose to use NAA maps for the voxel-wise group comparison. NAA is a characteristic peak in the brain proton spectra (Dezortova and Hajek, 2008) due to it being the second most abundant amino acid found in the brain (Dahmani *et al.*, 2021) contributing to its low CRLB. Therefore, NAA was assumed to have the highest probability of overlap between subjects due to the low number of voxels excluded during quality control. The largest cluster identified in the voxel-wise analysis of NAA was a region in the left thalamus where the NAA concentration was higher in the adolescents with PHIV than both the HEU and HUU groups combined (HIV-). However, no significant differences in NAA concentration level between HIV status groups were observed using the linear regression models in the left thalamus ROI. A possible explanation for this would be that the cluster detected was too small in comparison to the size of the left thalamus ROI that was considered during the linear regression analysis. This is plausible as the minimum left thalamus overlap of that we considered comprised approximately 260 voxels whereas the cluster identified by the voxel-wise analysis was 32 voxels. Consequently, the small size of the cluster relative to the left thalamus ROI may have diluted any statistical differences in NAA.

Choline is another robust metabolite peak in brain spectra, so voxel-wise analysis was also performed on glycerophosphocholine concentration maps. The largest clusters of altered glycerophosphocholine were located in the left and right thalamus where adolescents with PHIV showed higher glycerophosphocholine concentrations than the combined HEU and HUU group. Although the

increased glycerophosphocholine/tCr observed in the left thalamus using ROI analysis supports the results of the voxel-wise analysis, the lack of absolute glycerophosphocholine results in the left and right thalamus ROIs could, once again, be due to the small size of the cluster in comparison to the size of the thalamus. Alternatively, it could be the effect of confounders not controlled for in the voxel-wise analysis. These could include clinical measures, nutritional status such as BMI-for-age or maternal health indicators.

Despite the largest clusters being predominantly in the thalamus, clusters within the left caudate were also observed where the PHIV group had higher glycerophosphocholine than the HUU group. Although these clusters are small, the glycerophosphocholine concentration within these clusters may be considerably higher in adolescents with PHIV than the uninfected controls. As a result, this significant increase also reflects in the linear regression results showing increased glycerophosphocholine in the left caudate ROI in adolescents with PHIV relative to both the HUU groups and combined HEU and HUU groups.

Ins has high CRLB due to its difficulty in identifying and quantifying it from proton MRS spectra as it is not present in large amounts compared to NAA and spectrally overlaps other metabolites (Srinivasan *et al.*, 2004). There were several subjects who did not have a sufficient number of acceptable quality Ins voxels to be included in the study, meaning that a smaller number of subjects was included in the analysis of Ins that of the other metabolites. In addition, more voxels were excluded from each Ins map because they did not meet the quality criteria. This results in a low probability of voxel overlap between subjects; therefore, voxel-wise analysis was not attempted.

5.2. Effects of HIV exposure on brain metabolite levels in adolescents without HIV infection

In HEU adolescents, increased concentrations of Ins were observed in the left caudate and right thalamus when compared to the HUU adolescents. Furthermore, elevated Ins/tCr was also seen in the right thalamus.

In a study examining the effect HIV exposure without infection has on brain metabolites in children 2-3 years of age, increased Ins/tCr levels were observed (Bertran-Cobo *et al.*, 2022). The levels of the glial marker Ins/tCr typically increase and reaches a final value at which it plateaus during the first year after birth in a standard developing brain (Dezortova and Hajek, 2008; Bertran-Cobo *et al.*, 2022). Subsequently, Ins gradually declines with age (Dezortova and Hajek, 2008; Blüml *et al.*, 2013). Therefore, the elevated Ins/tCr levels seen at 2-3 years suggests an inflammatory response by the brain when exposed to HIV which may influence neurometabolic development in these children (Bertran-Cobo *et al.*, 2022). This is possible as just exposure to viral HIV particles can result in the

activation of microglia which, consequently, releases numerous soluble molecules such as chemokines, cytokines, and viral proteins like Tat. Tat has been shown to mediate mitochondrial dysfunction in microglia and, as a result, initiate and fuel chronic inflammation in microglia of which Ins is known to be a marker (Cotto, Natarajaseenivasan and Langford, 2019). This neuroinflammation is thought to persist into adolescence due to our findings of continued elevated Ins concentrations seen in both PHIV and HEU adolescents.

Contrastingly, no differences in Ins concentration levels were reported in the BG between HEU and HUU children at 7, 9 or 11 years of age (Robertson *et al.*, 2018; Graham *et al.*, 2020).

5.3. Methodological considerations

5.3.1. MRSI compared to conventional SVS

Presently, the majority of studies done on the effects of PHIV on children have been done using SVS, for example Keller *et al.* (2004); Mbugua *et al.* (2016); Holmes *et al.* (2017); Robertson *et al.* (2018); Graham *et al.* (2020) and van Biljon *et al.* (2021) with very little MRSI application seen (Van Dalen *et al.*, 2016; Salan *et al.*, 2023). SVS allows for the evaluation of changes in metabolites within a few selected anatomical brain regions whereas MRSI, by contrast, is capable of acquiring spectra from multiple voxels simultaneously in the 3D space, thereby allowing the creation of a spatial map of metabolite concentrations across a large brain volume of either the entire brain or specific regions of interest that can be isolated (Maudsley *et al.*, 2010). As a result, MRSI is more suitable for investigating and understanding changes in metabolite concentrations globally (Wilson *et al.*, 2019), such as in this case, where the effects of PHIV are not limited to one specific region.

At a wholistic viewpoint, both SVS and MRSI follow a similar methodology involving preprocessing, processing, analysis and quantification (Near *et al.*, 2021). In terms of region selection, SVS selects a single voxel in a specific brain region during acquisition from which a single voxel spectrum is generated. On the other hand, MRSI covers a larger VOI creating a data array with spectral information for multiple voxels in two or three dimensions (x, y and z). Thereafter, specific regions from the VOI can be chosen as the focus during analysis. This allows for greater flexibility in choosing multiple different ROIs at any stage. The preprocessing steps both include operations that remove or correct for spectral imperfections such eddy current and motion corrections (Near *et al.*, 2021). Both SVS and MRSI data may be co-registered to the T1-weighted structural image and segmented into different tissue types. However, MRSI may be used to generate metabolite maps and requires spatial transformation and spectral fitting considerations to separate signals from different regions (Zhang *et al.*, 2018; Wilson *et al.*, 2019).

5.3.2. Comparison of MRSI methods

MRSI studies have generally followed a similar methodological approach consisting of spectral and spatial acquisition, spatial reconstruction and spectral processing and fitting, followed by data analysis (Maudsley *et al.*, 2021). There are, however, variations within these individual steps that are suitable for different applications or research objectives that will be discussed.

Spectral and Spatial Acquisition

Many MRSI studies have utilised an EPSI sequence to acquire volumetric MRSI data (Maudsley *et al.*, 2010; Zhang *et al.*, 2018; Salan *et al.*, 2023). EPSI utilizes an oscillating readout gradient to obtain both spectral and spatial information simultaneously (Posse *et al.*, 1995). EPSI or spiral-encoding are common techniques for whole-brain acquisitions (Wilson *et al.*, 2019) as they accelerate the acquisition time, enabling a large volume to be covered with high spatial resolution in a feasible amount of time (Bogner *et al.*, 2014). Despite the accelerated acquisition achieved, using only EPSI to accelerate MRS acquisition time is not sufficient in completely avoiding motion artifacts and the extreme stresses placed on the gradient system, such as passive shims and the heating of gradient coils, that accompany EPSI (Ebel and Maudsley, 2003; Bogner *et al.*, 2014).

For volume-selective excitation, the LASER technique was used, as opposed to the conventional PRESS or STEAM excitations used for localized MRSI. This contrasts with EPSI acquisition which commonly uses non-selective excitation to excite the whole imaging volume (Posse *et al.*, 1995). However, LASER allows for significantly improved spatial selection accuracy involving reduced chemical shift errors, better selection profiles and B_1 field-insensitivity. Therefore, the combination of LASER excitation and spiral-encoded readout will be clinically significant (Andronesi *et al.*, 2010; Bogner *et al.*, 2014). However, volume-selective MRSI as used in our study limits the ability to cover cortical regions (Maudsley *et al.*, 2021). The LASER-localised spiral-encoded MRSI technique was also used by Ma *et al.* (2021) on which the atlas-based analysis approach used in this study is based. However, they combined LASER excitation and spiral encoding with the Mescher-Garwood (MEGA) spectral editing technique for GABA detection (Mescher *et al.*, 1998; Ma *et al.*, 2021).

MRSI Processing

An automated atlas-based approach similar to that used by (Ma *et al.*, 2021) was utilized in this study to quantify average metabolite concentrations within specific ROIs, namely the caudate and thalamus. Our approach differs slightly from their atlas-based approach in that we used nearest neighbour interpolation to obtain high resolution metabolite maps. Furthermore, we obtained an average caudate coverage of 80% and thalamus coverage of approximately 50% (Table 4.3) which is less than the 100% thalamic overlap achieved by Ma *et al.* (2021). Therefore, in our study this approach may

not provide as good a representation of thalamus metabolite levels. Ma *et al.* (2021) found that the atlas-based approach showed high reproducibility due to better ROI definition compared to manual selection of a predefined number of voxels within the region. Because the volume definition of the atlas ROI is more accurate, the averaged neurometabolic levels calculated better represent those of the entire region. By contrast, manual selection of voxels results in more variable metabolite concentrations due to the possible selection of sub-structures within the ROI that represent only a small portion of the region (Ma *et al.*, 2021). However, despite not achieving 100% overlap with the atlas ROIs, the current study demonstrates the feasibility of an atlas-based approach for quantifying and processing MRSI data within specific brain regions which can then be used to better analyse results from clinical applications, such as investigating group differences in metabolites between adolescents with and without PHIV.

MRSI was also used by Van Dalen *et al.* (2016) with some similarities and some differences in methodology compared to our study. Their acquisition differed from ours in that they used PRESS as opposed to LASER localization and acquired MR spectra from 1 axial slice. They similarly segmented GM and WM using the T1-weighted structural image and quantified the metabolite spectra using LCModel. However, they averaged metabolite levels within GM and WM voxels to obtain GM and WM mean values (Van Dalen *et al.*, 2016). This was performed over a large VOI and did not consider specific structures within the GM or WM, which is an advantageous feature of the ROI approach we used. This is due to the risk associated with assessing large areas in which smaller regional variations may be masked (Van Dalen *et al.*, 2016). Using the ROI approach, specifically defined structures can be examined and identified for regional differences.

Several open-source software packages and scripts have been developed to aid in MRSI processing. LCModel, a commonly-used MRS data quantification tool, was used in the current study to estimate metabolite concentrations and their ratios to tCr in a similar way to Ma *et al.* (2021). The MIDAS (Metabolite Imaging and Data Analysis System) software (Maudsley *et al.*, 2006) can perform whole-brain MRSI data visualization, processing and analysis. This package offers an integrated set of MRSI processing functions including metabolite map generation, spectral quality control, CSF fraction calculation and registration and is, therefore, used in many MRSI studies (Maudsley *et al.*, 2010; Zhang *et al.*, 2018; Salan *et al.*, 2023). However, it is intended for analysis of data acquired with the EPSI sequence (Bogner, Otazo and Henning, 2021) and is written in Interactive Data Language (IDL) which is not free or easily accessible. Oryx-MRSI does not provide spectral fitting functionality but offers similar map generation and visualisation capabilities. Furthermore, Oryx-MRSI is able to load and visualize files generated by LCModel, a beneficial feature as LCModel is a widely used spectral analysis

program that is often considered the gold standard for MRS data and was used for spectral fitting in this study. As the Oryx-MRSI software is written in MATLAB, it is easily accessible and adjustable.

Oryx-MRSI also loads and displays NIfTI-MRS file types, which is an uncommon feature missing in most processing software (Cengiz *et al.*, 2022). The establishment of standardized MRS and MRSI data formats has lagged behind those for MR imaging. NIfTI-MRS is a very recent development and so processing is not yet included in MRS processing software (Clarke *et al.*, 2022). The NIfTI file format was chosen as it is the standard for functional, anatomical, quantitative and diffusion MRI storage. By aligning MRSI data with this format, different modalities can be integrated easily (Clarke *et al.*, 2022).

We therefore used Oryx-MRSI because of the broad functionality it offered which suited our needs. However, it did not offer all the functionality we required to process our data. For instance, despite being able to load and display NIfTI-MRS data, we had to make modifications to allow these data to be processed and to create metabolite maps. Furthermore, complete tissue corrections were not applied as only corrections for CSF were included. Thus, we developed the complete corrections and added it to the software code. We, therefore, used Oryx-MRSI as a base and altered the necessary modules to create a modified processing pipeline that applied to our dataset and can be used in future studies using MRSI.

Data Analysis

MRS studies investigating the effect of PHIV on children have predominantly used multiple linear regression analyses on metabolite levels from single voxels (Holmes *et al.*, 2017; Robertson *et al.*, 2018) as it is effective for comparison of metabolite concentration levels between groups with different HIV statuses (Montgomery, Peck and Vining, 2012). Such studies have acquired data from single voxels in specific regions and analysed the metabolite changes within these voxels independently of each other. This method, however, has its limitations in that it prevents a wholistic understanding of metabolite relationship dynamics across different brain regions from being considered (Yiannoutsos *et al.*, 2004). Therefore, to analyse the impact of HIV on both inter-metabolite and inter-regional relationships, other methods can be applied, such as factor analysis in which patterns between variables can be identified based on their correlations (Yiannoutsos *et al.*, 2004; Graham *et al.*, 2020).

In MRSI, a simple and frequently used approach has been to manually select a few voxels representing the ROI to be analysed. This can lead to inaccuracies that are addressed with the ROI approach used in this study. Extracting all voxels belonging to the particular ROI for comparison once registered to standard MNI space ensures the same anatomical region is covered in all subjects. This analysis method is supported due to the image format of MRSI (Maudsley *et al.*, 2021).

Investigations have been done on the application of not only univariate, but also multivariate voxel-wise analysis using MRSI data (Young *et al.*, 2010). This is possible because MRSI provides simultaneous measurement of multiple metabolites for each voxel. Such analysis may reveal inter-metabolite relationships that are missed using a univariate approach. In simulation studies, the multivariate approach was found to provide more statistical power for detecting metabolite changes when there is a joint metabolite effect compared to the univariate approach. However, this improvement is only present when the joint metabolite effect is substantial, which may not be known prior to analysis (Young *et al.*, 2010). The appropriate choice of approach is also governed by the research question. Univariate analysis identifies changes in any given metabolite and is the aim of this study. Multivariate analysis can identify overall inter-metabolites interactions and correlations which, though not considered in this study, could be used in future works.

5.3.3. Comparison between MRSI and SLIM methods

Despite the improvements MRSI offers, there are still limitations stemming from partial volume of different tissue types and point spread function effects (Adany, Choi and Lee, 2016) as well as a strong B_0 inhomogeneity (Donadieu *et al.*, 2016). To address partial volume affects, we used a tissue correction method. Fractional tissue maps of GM, WM and CSF were created and used to account for the heterogenous tissue composition in each voxel. This included using tissue-specific values for water concentration and relaxation factors.

In this application, as we are focusing on specific ROIs and not a whole-brain analysis, the SLIM method may offer even more accurate results. When comparing MRSI and SLIM methods using the same k-space size, SLIM was found to achieve significant improvements in inter-voxel signal contamination (Hu *et al.*, 1988; Lee, Adany and Choi, 2017). This is as SLIM obtains spectra from compartments of homogeneous tissue using arbitrary shapes, thus, eliminating partial volume effects. Yet, SLIM is still subject to errors as a result of inhomogeneous B_0 and B_1 fields. The application of a B_0-adjusted SLIM (BSLIM) method can offer a solution to this problem (Adany, Choi and Lee, 2016). However, to perform the BSLIM method, a B_0 field inhomogeneity map is required (Khalidov *et al.*, 2006). As neither B_0 nor B_1 maps were acquired at time of scanning, this method could not be implemented in this study.

6. Conclusion

In conclusion, as hypothesized, elevated glycerophosphocholine concentrations were observed in the left caudate of adolescents with PHIV at 15 years compared to the uninfected controls. Additionally, elevated Ins concentrations and GPC/tCr were found in the thalamus bilaterally in adolescents with PHIV. Both results, together, indicate ongoing inflammation in the BG of adolescents with PHIV despite early ART initiation. These findings are consistent with those observed in a longitudinal study examining this cohort at younger ages which further supports the connection between increased choline levels and persistent inflammation found in the BG throughout childhood and into adolescence.

Furthermore, the voxel-wise approach identified significant clusters of elevated glycerophosphocholine in the thalamus and caudate in the adolescents with PHIV relative to uninfected controls. Such findings show consistency between the different analysis approaches thus verifying the feasibility of the MRSI technique in this application.

7. Limitations and future work

A limitation of this study is that, despite providing insight into neurometabolic changes occurring in adolescents with PHIV, we are unable to determine whether these changes are a result of HIV or the effects of ART. Furthermore, the relationship between viral load and metabolite concentration as well as intra-regional metabolite correlations were not considered and could, therefore, be explored in future studies. Only GPC was considered and not tCho as is usually done in MRS studies due to the basis set used and is, therefore, a limitation of this study.

As this is the first study to investigate this cohort of children at 15 years, it can form a basis for expansion in future work. This could include performing an analysis across a wider region covered by the MRSI acquisition to identify other possible regions of differing metabolite concentrations. Additionally, the association of these metabolic changes with cognitive performance can be investigated to determine if and how these are related, especially since the BG is significantly involved in both motor control and language processing (Booth *et al.*, 2007).

The nature of this study is cross-sectional as metabolic differences between the different HIV status groups were examined at only one timepoint. Using a longitudinal approach, neurometabolic changes can be investigated at multiple ages to identify trends in metabolic levels and disease progression over time. Since MRSI data was acquired at 2 adolescent timepoints, future work could look at longitudinal analysis of MRSI data during adolescence. Results obtained from MRSI could also be compared to

those obtained using SVS in the same participants. A sophisticated longitudinal analysis could incorporate metabolite concentrations obtained from both methods at different ages.

An atlas-based MRSI approach was utilized in this study, of which the results were validated using a voxel-wise between group comparison method. This has established a processing pipeline that can be used in future studies. Future work could include partial volume regression where tissue-specific metabolite concentrations can be obtained by expressing the measured metabolite concentration at each voxel as the partial volume-weighted sum of tissue-specific metabolite concentrations and solving an overdetermined system of equations. This may result in a higher sensitivity for detecting metabolic differences between HIV status groups. Metabolite relaxation times were not considered due to short TE and long TR times and to avoid possibly incorrect assumptions about relaxation times and could be investigated in future studies. We also did not consider the MRSI point spread function or chemical shift effects, though we expect these effects to be small (Ma *et al.*, 2021; Öz *et al.*, 2023). We were not able to explore the SLIM method as B_0 and B_1 field maps were not acquired during scanning. This could be a consideration for future acquisitions.

Finally, it would be interesting to investigate brain differences resulting from PHIV using different MRI modalities at 15 years. Despite our findings being largely consistent with those found at younger and older ages (van Biljon *et al.*, 2021; Salan *et al.*, 2023), MRSI analysis alone is not enough to draw definitive conclusions on the effect of PHIV on the developing brain. Therefore, additional studies exploring structural and functional changes at this age group could be tied to these spectroscopic findings which may offer a more wholistic view on PHIV and early ART effects. This will also provide more insight into the meaning of the neurometabolic changes in terms of structural or signalling pathway alterations.

8. References

Adany, P., Choi, I.Y. and Lee, P. (2016) 'B0-adjusted and sensitivity-encoded spectral localization by imaging (BASE-SLIM) in the human brain in vivo', *NeuroImage*, 134, pp. 355–364. doi:10.1016/j.neuroimage.2016.04.016.

An, L., Warach, S. and Shen, J. (2011) 'Spectral Localization by Imaging Using Multi-Element Receiver Coils', *Magnetic Resonance in Medicine* [Preprint]. doi:10.1002/mrm.22783.

Ananworanich, J. *et al.* (2016) 'Neurocognition and quality of life after reinitiating antiretroviral therapy in children randomized to planned treatment interruption', *Aids*, 30(7), pp. 1075–1081. doi:10.1097/QAD.0000000000001011.

Andronesi, O.C. *et al.* (2010) 'Spectroscopic imaging with improved gradient modulated constant adiabaticity pulses on high-field clinical scanners', *Journal of Magnetic Resonance*, 203(2), pp. 283–293. doi:10.1016/j.jmr.2010.01.010.

Arts, E.J. and Hazuda, D.J. (2012) 'HIV-1 antiretroviral drug therapy', *Cold Spring Harbor Perspectives in Medicine*, 2(4). doi:10.1101/cshperspect.a007161.

Ashburner, J. *et al.* (2013) 'SPM12 Manual The FIL Methods Group (and honorary members)', *Functional Imaging Laboratory*, pp. 475–1.

Ashby, J. *et al.* (2015) 'Cerebral function in perinatally HIV-infected young adults and their HIV-uninfected sibling controls', *HIV Clinical Trials*, 16(2), pp. 81–87. doi:10.1179/1528433614Z.0000000003.

Bertran-Cobo, C. *et al.* (2022) 'A Neurometabolic Pattern of Elevated Myo-Inositol in Children Who Are HIV-Exposed and Uninfected: A South African Birth Cohort Study', *Frontiers in Immunology*, 13(March), pp. 1–14. doi:10.3389/fimmu.2022.800273.

van Biljon, N. *et al.* (2021) 'Multivariate approach for longitudinal analysis of brain metabolite levels from ages 5-11 years in children with perinatal HIV infection', *NeuroImage*, 237(March). doi:10.1016/j.neuroimage.2021.118101.

Bjartmar, C. *et al.* (2002) 'N-acetylaspartate is an axon-specific marker of mature white matter in vivo: A biochemical and immunohistochemical study on the rat optic nerve', *Annals of Neurology*, 51(1), pp. 51–58. doi:10.1002/ana.10052.

Blüml, S. *et al.* (2013) 'Metabolic maturation of the human brain from birth through adolescence: insights from in vivo magnetic resonance spectroscopy.', *Cerebral cortex (New York, N.Y. : 1991)*,

23(12), pp. 2944–2955. doi:10.1093/cercor/bhs283.

Bogner, W. *et al.* (2014) 'Real-time motion- and B 0 -correction for LASER-localized spiral-accelerated 3D-MRSI of the brain at 3 T', *NeuroImage*, 88, pp. 22–31. doi:10.1016/j.neuroimage.2013.09.034.

Bogner, W., Otazo, R. and Henning, A. (2021) 'Accelerated MR spectroscopic imaging—a review of current and emerging techniques', *NMR in Biomedicine*, 34(5), pp. 1–32. doi:10.1002/nbm.4314.

Boivin, M.J. *et al.* (2019) 'Neuropsychological performance in African children with HIV enrolled in a multi-site anti-retroviral clinical trial', 32(2), pp. 189–204. doi:10.1097/QAD.0000000000001683.Neuropsychological.

Booth, J.R. *et al.* (2007) 'The role of the basal ganglia and cerebellum in language processing', *Brain Research*, 1133(1), pp. 136–144. doi:10.1016/j.brainres.2006.11.074.

Borrajo, A. *et al.* (2021) 'Crucial role of central nervous system as a viral anatomical compartment for hiv-1 infection', *Microorganisms*, 9(12), pp. 1–22. doi:10.3390/microorganisms9122537.

Braissant, O. *et al.* (2005) 'Creatine synthesis and transport during rat embryogenesis: Spatiotemporal expression of AGAT, GAMT and CT1', *BMC Developmental Biology*, 5, pp. 1–16. doi:10.1186/1471-213X-5-9.

Cecil, K.M. (2013) 'Proton Magnetic Resonance Spectroscopy: Technique for the Neuroradiologist', *Neuroimaging Clinics of North America*, 23(3), pp. 381–392. doi:10.1016/j.nic.2012.10.003.

Cengiz, S. *et al.* (2022) 'ORYX-MRSI: A fully-automated open-source software for proton magnetic resonance spectroscopic imaging data analysis', *International Journal of Imaging Systems and Technology*, 32(4), pp. 1068–1083. doi:10.1002/ima.22748.

Chang, L. *et al.* (2003) 'Persistent brain abnormalities in antiretroviral-naive HIV patients 3 months after HAART', *Antiviral Therapy*, 8(1), pp. 17–26. doi:10.1177/135965350300800103.

Chang, L. *et al.* (2013) 'Magnetic Resonance Spectroscopy to Assess NeuroInflammation and Neuropathic Pain', *J Neuroimmune Pharmacology* [Preprint]. doi:10.1007/s11481-013-9460-x.

Clarke, W. *et al.* (2022) *NIfTI-MRS: A standard data format for magnetic resonance spectroscopy*, *Magnetic Resonance Medical*. Available at: https://github.com/wtclarke/spec2nii.

Cohen, S. *et al.* (2016) 'Cerebral injury in perinatally HIV-infected children compared to matched healthy controls', *Neurology*, 86(1), pp. 19–27. doi:10.1212/WNL.0000000000002209.

Cotto, B., Natarajaseenivasan, K. and Langford, D. (2019) 'HIV infection alters energy metabolism in

the brain: contributions to HIV-associated neurocognitive disorders', pp. 1–24. doi:10.1016/j.pneurobio.2019.101616.HIV.

Cotton, M. *et al.* (2013) 'Early limited antiretroviral therapy is superior to deferred therapy in HIV-infected South African infants: results from the CHER (Children with HIV Early antiRetroviral) Randomized Trial', *Lancet*, pp. 1555–1563. doi:10.1016/S0140-6736(13)61409-9.Early.

Dahmani, S. *et al.* (2021) 'Alterations of Brain Metabolites in Adults With HIV: A Systematic Meta-analysis of Magnetic Resonance Spectroscopy Studies', *Neurology*, 97(11), pp. E1085–E1096. doi:10.1212/WNL.0000000000012394.

Daikhin, Y. and Yudkoff, M. (2000) 'Compartmentation of brain glutamate metabolism in neurons and glia', *Journal of Nutrition*, 130(4 SUPPL.), pp. 1026–1031. doi:10.1093/jn/130.4.1026s.

Van Dalen, Y.W. *et al.* (2016) 'Neurometabolite alterations associated with cognitive performance in perinatally HIV-infected children', *Medicine (United States)*, 95(12), pp. 1–10. doi:10.1097/MD.0000000000003093.

Dezortova, M. and Hajek, M. (2008) '1H MR spectroscopy in pediatrics', *European Journal of Radiology*, 67(2), pp. 240–249. doi:10.1016/j.ejrad.2008.02.035.

Le Doaré, K., Bland, R. and Newell, M.L. (2012) 'Neurodevelopment in children born to HIV-infected mothers by infection and treatment status', *Pediatrics*, 130(5). doi:10.1542/peds.2012-0405.

Donadieu, M. *et al.* (2016) 'Metabolic voxel-based analysis of the complete human brain using fast 3D-MRSI: Proof of concept on Multiple Sclerosis', *Magnetic Resonance Imaging*, pp. 411–419. doi:10.1002/jmri.25139.

Dumontheil, I. (2016) 'Adolescent brain development', *Current Opinion in Behavioral Sciences*, 10, pp. 39–44. doi:10.1016/j.cobeha.2016.04.012.

Ebel, A. and Maudsley, A.A. (2003) 'Improved spectral quality for 3D MR spectroscopic imaging using a high spatial resolution acquisition strategy', *Magnetic Resonance Imaging*, 21(2), pp. 113–120. doi:10.1016/S0730-725X(02)00645-8.

Ellis, R.J., Calero, P. and Stockin, M.D. (2009) 'HIV infection and the central nervous system: A primer', *Neuropsychology Review*, 19(2), pp. 144–151. doi:10.1007/s11065-009-9094-1.

Ellis, S., Yang, X. and Fischer, K. (2019) 'Quantitative Assessment of Magnetic Resonance Spectroscopy Data Reconstruction Methods: Region-of-Interest Averaging and Spectral Localization by Imaging', (May). Available at: https://kuscholarworks.ku.edu/handle/1808/29700.

Ene, L., Duiculescu, D. and Ruta, S.M. (2011) 'How much do antiretroviral drugs penetrate into the central nervous system?', *Journal of medicine and life*, 4(4), pp. 432–439.

Fisher, S.K., Novak, J.E. and Agranoff, B.W. (2002) 'Inositol and higher inositol phosphates in neural tissues: Homeostasis, metabolism and functional significance', *Journal of Neurochemistry*, 82(4), pp. 736–754. doi:10.1046/j.1471-4159.2002.01041.x.

Flynn, P.M. and Abrams, E.J. (2019) 'Growing up with perinatal HIV', *Aids*, 33(4), pp. 597–603. doi:10.1097/QAD.0000000000002092.

Gamage, R. *et al.* (2020) 'Cholinergic Modulation of Glial Function During Aging and Chronic Neuroinflammation', *Frontiers in Cellular Neuroscience*, 14(October), pp. 1–26. doi:10.3389/fncel.2020.577912.

Gasparovic, C. *et al.* (2006) 'Use of tissue water as a concentration reference for proton spectroscopic imaging', *Magnetic Resonance in Medicine*, 55(6), pp. 1219–1226. doi:10.1002/mrm.20901.

Ghosh, A.K., Sarkar, A. and Mitsuya, H. (2017) 'HIV-Associated Neurocognitive Disorder (HAND) and the Prospect of Brain-Penetrating Protease Inhibitors for Antiretroviral Treatment', *Medical Research Archives* [Preprint].

Giedd, J.N. *et al.* (1999) 'Brain development during childhood and adolescence: A longitudinal MRI study [2]', *Nature Neuroscience*, 2(10), pp. 861–863. doi:10.1038/13158.

Giedd, J.N. *et al.* (2006) 'Anatomic Brain Imaging Studies of Normal and Abnormal Brain Development in Children and Adolescents', *Developmental Psychopathology* [Preprint]. doi:10.1002/9780470939390.ch3.

Gnanakaran, S. *et al.* (2007) 'Clade-Specific Differences between Human Immunodeficiency Virus Type 1 Clades B and C: Diversity and Correlations in C3-V4 Regions of gp120', *Journal of Virology*, 81(9), pp. 4886–4891. doi:10.1128/jvi.01954-06.

Gonzalez-Scarano, F. and Martin-Garcia, J. (2005) 'The neuropathogenesis of AIDS', *Nature Reviews, Immunology* [Preprint]. doi:10.1038/nri1527.

Gorman, A. *et al.* (2009) 'Functional Consequences of HIV-Associated Neuropsychological Impairment', *Neuropsychology Review* [Preprint]. doi:10.1007/s11065-009-9095-0.Functional.

Goryawala, M.Z. *et al.* (2018) 'Spectral Decomposition for Resolving Partial Volume Effects in MRSI', *Magnetic Resonance Medical*, pp. 2886–2895. doi:10.1002/mrm.26991.Spectral.

Govindaraju, V., Young, K. and Maudsley, A.A. (2000) 'Proton NMR chemical shifts and coupling

constants for brain metabolites', *NMR in Biomedicine*, 13(3), pp. 129–153. doi:10.1002/1099-1492(200005)13:3<129::AID-NBM619>3.0.CO;2-V.

De Graaf, R.A. (2007) *In Vivo NMR Spectroscopy - 2nd Edition Principles and Techniques*, *Journal of Animal Science*.

Graham, A.S. *et al.* (2020) 'MRS suggests multi-regional inflammation and white matter axonal damage at 11 years following perinatal HIV infection', *NeuroImage: Clinical*, 28(November), p. 102505. doi:10.1016/j.nicl.2020.102505.

Graybiel, A.M. (2004) 'Network-level neuroplasticity in cortico-basal ganglia pathways', *Parkinsonism and Related Disorders*, 10(5), pp. 293–296. doi:10.1016/j.parkreldis.2004.03.007.

Hansson, E. and Ronnback, L. (2003) 'Glial neuronal signaling in the central nervous system', *FASEB Journal* [Preprint]. doi:10.1096/fj.02-0429rev.

Harezlak, J. *et al.* (2011) 'Persistence of HIV-associated cognitive impairment, inflammation, and neuronal injury in era of highly active antiretroviral treatment', *Aids*, 25(5), pp. 625–633. doi:10.1097/QAD.0b013e3283427da7.

Hoare, J. *et al.* (2014) 'Systematic review of neuroimaging studies in vertically transmitted HIV positive children and adolescents', *Metabolic Brain Disease*, 29(2), pp. 221–229. doi:10.1007/s11011-013-9456-5.

Hoare, J. *et al.* (2015) 'White matter micro-structural changes in ART-naive and ART-treated children and adolescents infected with HIV in South Africa', *Aids*, 29(14), pp. 1793–1801. doi:10.1097/QAD.0000000000000766.

Holmes, M.J. *et al.* (2017) 'Longitudinal increases of brain metabolite levels in 5-10 year old children', *PLoS ONE*, 12(7), pp. 1–14. doi:10.1371/journal.pone.0180973.

Horn, P.S. *et al.* (2001) 'Effect of outliers and nonhealthy individuals on reference interval estimation', *Clinical Chemistry*, 47(12), pp. 2137–2145. doi:10.1093/clinchem/47.12.2137.

Hu, X. *et al.* (1988) 'SLIM: Spectral Localization by Imaging', *Magnetic Resonance in Medicine* [Preprint]. doi:10/1002/mrm.1910080308.

Irshad, U., Mahdy, H. and Tonismae, T. (2022) *HIV in Pregnancy*, *Treasure Island (FL): StatPearls Publishing*. Available at: https://www.ncbi.nlm.nih.gov/books/NBK558972/.

Keller, M.A. *et al.* (2004) 'Altered neurometabolite development in HIV-infected children: Correlation with neuropsychological tests', *Neurology*, 62(10), pp. 1810–1817.

doi:10.1212/01.WNL.0000125492.57419.25.

Khalidov, I. *et al.* (2006) 'Improved MRSI with field inhomogeneity compensation', *Medical Imaging 2006: Image Processing*, 6144, p. 614467. doi:10.1117/12.651868.

Kirchner, T. *et al.* (2015) 'Reduction of voxel bleeding in highly accelerated parallel 1H MRSI by direct control of the spatial response function', *Magnetic Resonance in Medicine*, 73(2), pp. 469–480. doi:10.1002/mrm.25185.

Kries, R., Ernst, T. and Ross, B.D. (1993) 'Absolute quantitation of water and metabolites in the human brain. II. Metabolite concentrations.', *Journal of Magnetic Resonance Imaging* [Preprint]. doi:10.1006/jmrb.1993.1056.

Laughton, B. *et al.* (2013) 'Neurodevelopment in perinatally HIV-infected children: A concern for adolescence', *Journal of the International AIDS Society*, 16. doi:10.7448/IAS.16.1.18603.

Laughton, B. *et al.* (2018) 'Five year neurodevelopment outcomes of perinatally HIV-infected children on early limited or deferred continuous antiretroviral therapy', *Journal of the International AIDS Society*, 21(5), p. e25106. doi:10.1002/jia2.25106.

Lee, P., Adany, P. and Choi, I.Y. (2017) 'Imaging based magnetic resonance spectroscopy (MRS) localization for quantitative neurochemical analysis and cerebral metabolism studies', *Analytical Biochemistry*, 529, pp. 40–47. doi:10.1016/j.ab.2017.01.007.

Leisman, G., Braun-Benjamin, O. and Melillo, R. (2014) 'Cognitive-motor interactions of the basal ganglia in development', *Frontiers in Systems Neuroscience*, 8(FEB), pp. 1–18. doi:10.3389/fnsys.2014.00016.

Lewis-de los Angeles, C.P. *et al.* (2016) 'Deformed Subcortical Structures Are Related to Past HIV Disease Severity in Youth With Perinatally Acquired HIV Infection', *Journal of the Pediatric Infectious Diseases Society*, 5, pp. S6–S14. doi:10.1093/jpids/piw051.

Li, B.S.Y., Wang, H. and Gonen, O. (2003) 'Metabolite ratios to assumed stable creatine level may confound the quantification of proton brain MR spectroscopy', *Magnetic Resonance Imaging*, 21(8), pp. 923–928. doi:10.1016/S0730-725X(03)00181-4.

Li, X. *et al.* (2016) 'The first step for neuroimaging data analysis: DICOM to NIfTI conversion', *J Neurosci Methods* [Preprint]. doi:10.1016/j.jneumeth.2016.03.001.

Li, X. *et al.* (2017) 'Generation of a whole-brain atlas for the cholinergic system and mesoscopic projectome analysis of basal forebrain cholinergic neurons', *Proceedings of the National Academy of*

Sciences of the United States of America, 115(2), pp. 415–420. doi:10.1073/pnas.1703601115.

Li, X. *et al.* (2022) 'The Distribution of Major Brain Metabolites in Normal Adults: Short Echo Time Whole-Brain MR Spectroscopic Imaging Findings', *Metabolites*, 12(6). doi:10.3390/metabo12060543.

Lorin, V. *et al.* (2020) 'Antibody Neutralization of HIV-1 Crossing the Blood-Brain Barrier', *American Society for Microbiology*, 11(5).

Lu, H. *et al.* (2005) 'Routine clinical brain MRI sequences for use at 3.0 tesla', *Journal of Magnetic Resonance Imaging*, 22(1), pp. 13–22. doi:10.1002/jmri.20356.

Ma, R. *et al.* (2021) 'Atlas-based GABA-mapping with 3D MEGA-MRSI: Cross-correlation to single voxel MRS'. doi:10.1002/nbm.4275.Atlas-based.

Mansfield, P. (1984) 'Spatial mapping of the chemical shift in NMR', *Magnetic Resonance in Medicine* [Preprint].

Maudsley, A.A. *et al.* (2006) 'Comprehensive processing, display and analysis for in vivo MR spectroscopic imaging', *NMR Biomedical* [Preprint]. doi:10.1016/B978-044452701-1.00004-1.

Maudsley, A.A. *et al.* (2010) 'Mapping of Brain Metabolite Distributions by Volumetric Proton.pdf', 61(3), pp. 548–559. doi:10.1002/mrm.21875.Mapping.

Maudsley, A.A. *et al.* (2021) 'Advanced magnetic resonance spectroscopic neuroimaging: Experts' consensus recommendations', pp. 1–37. doi:10.1002/nbm.4309.Advanced.

Mbugua, K.K. *et al.* (2016) 'HIV-associated CD4+/CD8+ depletion in infancy is associated with neurometabolic reductions in the basal ganglia at age 5 years despite early antiretroviral therapy', *Aids*, 30(9), pp. 1353–1362. doi:10.1097/QAD.0000000000001082.

Melrose, R.J. *et al.* (2008) 'Compromised fronto-striatal functioning in HIV: An fMRI investigation of semantic event sequencing', *Behavioural Brain Research*, 188(2), pp. 337–347. doi:10.1016/j.bbr.2007.11.021.

Mescher, M. *et al.* (1998) 'Simultaneous in vivo spectral editing and water suppression', *NMR in Biomedicine* [Preprint]. doi:10.1002/(sici)1099-1492(199810)11:6<266::aid-nbm530>3.0.co;2-j.

Mofenson, L.M. and Cotton, M.F. (2013) 'The challenges of success: Adolescents with perinatal HIV infection', *Journal of the International AIDS Society*, 16, pp. 15–17. doi:10.7448/IAS.16.1.18650.

Moffett, J.R. *et al.* (2007) 'N-Acetylaspartate in the CNS: From neurodiagnostics to neurobiology', *Progress in Neurobiology*, 81(2), pp. 89–131. doi:10.1016/j.pneurobio.2006.12.003.

Montgomery, D.C., Peck, E.A. and Vining, G.G. (2012) *Introduction to Linear Regression Analysis*.

Mzingwane, M. and Tiemessen, C. (2017) 'Mechanisms ofHIV persistence in HIV reservoirs', *Rev Med Virol* [Preprint]. doi:https://doi.org/10.1002/rmv.1924.

Nath, A. (2015) 'Eradication of human immunodeficiency virus from brain reservoirs', *Journal of NeuroVirology*, 21(3), pp. 227–234. doi:10.1007/s13365-014-0291-1.

Near, J. *et al.* (2021) 'Preprocessing, analysis and quantification in single-voxel magnetic resonance spectroscopy: Experts' consensus recommendations', *NMR Biomedical* [Preprint]. doi:10.1002/nbm.4257.

Newell, M. *et al.* (2004) 'Mortality of infected and uninfected infants born to HIV-infected mothers in Africa: a pooled analysis', *Lancet* [Preprint]. doi:10.1016/S0140-6736(04)17140-7.

Nichols, S.L. *et al.* (2015) 'Executive Functioning in Children and Adolescents With Perinatal HIV Infection', *Pediatric Infectious Disease Journal*, 34(9), pp. 969–975. doi:10.1097/INF.0000000000000809.

Novak, J.. *et al.* (1999) 'Differentiated Human NT2-N Neurons Possess a High Intracellular Content of myo-Inositol', *Journal of Neurochemistry*, pp. 1431–1440. doi:10.1046/j.1471-4159.1999.721431.x.

Nwosu, E.C. *et al.* (2019) 'Altered brain morphometry in 7-year old HIV-infected children on early ART', 33(2), pp. 523–535. doi:10.1007/s11011-017-0162-6.Altered.

Oeltzschner, G. *et al.* (2021) 'Osprey: Open-Source Processing, Reconstruction & Estimation of Magnetic Resonance Spectroscopy Data', pp. 1–27. doi:10.1016/j.jneumeth.2020.108827.Osprey.

de Oliveira, F.T.M. (2015) 'Central Nervous System Antiretroviral High Penetration Therapy', *Journal of AIDS & Clinical Research*, 06(12), pp. 10–13. doi:10.4172/2155-6113.1000529.

Öz, G. *et al.* (2023) 'MR Imaging in Ataxias: Consensus Recommendations by the Ataxia Global Initiative Working Group on MRI Biomarkers', *Cerebellum* [Preprint], (0123456789). doi:10.1007/s12311-023-01572-y.

Pfefferbaum, A. *et al.* (2012) 'Regional Brain Structural Dysmorphology in HIV infection: Effects of AIDS, Alcoholism, and Age.', *Biol Psychiatry*, 72(5), pp. 361–370. doi:10.1016/j.biopsych.2012.02.018.Regional.

Phillips, N. *et al.* (2016) 'HIV-associated cognitive impairment in perinatally infected children: A meta-analysis', *Pediatrics*, 138(5). doi:10.1542/peds.2016-0893.

Phillips, N.J. *et al.* (2018) 'HIV-associated cognitive disorders in perinatally infected children and adolescents: a novel composite cognitive domains score', *AIDS Care - Psychological and Socio-Medical Aspects of AIDS/HIV*, 30, pp. 8–16. doi:10.1080/09540121.2018.1466982.

Piechnik, S.K. *et al.* (2009) 'Functional changes in CSF volume estimated using measurement of water T2 relaxation', *Magnetic Resonance in Medicine*, 61(3), pp. 579–586. doi:10.1002/mrm.21897.

Podo, F. (1999) 'Tumour phospholipid metabolism', *NMR in Biomedicine* [Preprint]. doi:10.1002/(sici)1099-1492(199911)12:7<413::aid-nbm587>3.0co;2-u.

Posse, S. *et al.* (1995) 'High speed 1H spectroscopic imaging in human brain by echo planar spatial-spectral encoding', *Magnetic Resonance in Medicine* [Preprint]. doi:10.1002/mrm.1910330106.

Provencher, S.W. (2001) 'Automatic quantitation of localized in vivo 1H spectra with LCModel', *NMR in Biomedicine*, 14(4), pp. 260–264. doi:10.1002/nbm.698.

Qi, S. *et al.* (2015) 'Cerebral metabolism in HIV infected patients with non-cognitive disorder using single voxel magnetic resonance spectroscopy', *Radiology of Infectious Diseases*, 2(2), pp. 61–64. doi:10.1016/j.jrid.2015.06.004.

Quadrelli, S., Mountford, C. and Ramadan, S. (2016) 'Hitchhiker'S Guide to Voxel Segmentation for Partial Volume Correction of in Vivo Magnetic Resonance Spectroscopy', *Magnetic Resonance Insights*, 9(April), p. MRI.S32903. doi:10.4137/mri.s32903.

R Core Team (2020) *R: A Language and Environment for Statistical Computing*, *R Foundation for Statistical Computing*. Available at: http://www.r-project.org.

Rae, C.D. (2014) 'A guide to the metabolic pathways and function of metabolites observed in human brain 1H magnetic resonance spectra', *Neurochemical Research*, 39(1), pp. 1–36. doi:10.1007/s11064-013-1199-5.

Randall, S.R. *et al.* (2017) 'Larger subcortical gray matter structures and smaller corpora callosa at age 5 years in HIV infected children on early ART', *Frontiers in Neuroanatomy*, 11(November). doi:10.3389/fnana.2017.00095.

Robertson, F.C. *et al.* (2018) 'Perinatal HIV infection or exposure is associated with low n-acetylaspartate and glutamate in basal ganglia at age 9 but not 7 years', *Frontiers in Human Neuroscience*, 12(May), pp. 1–10. doi:10.3389/fnhum.2018.00145.

Rowe, K. *et al.* (2023) 'The adolescent HIV executive function and drumming (AHEAD) study, a feasibility trial of a group drumming intervention amongst adolescents with HIV', *AIDS Care -*

Psychological and Socio-Medical Aspects of AIDS/HIV [Preprint]. doi:10.1080/09540121.2023.2195607.

Ruiz-Cabello, J. and Cohen, J.S. (1992) 'Phospholipid metabolites as indicators of cancer cell function', *NMR in Biomedicine* [Preprint]. doi:10.1002/nbm.1940050506.

Salan, T. *et al.* (2023) 'Whole-brain MR spectroscopic imaging reveals regional metabolite abnormalities in perinatally HIV infected young adults', *Frontiers in Neuroscience*, 17(March). doi:10.3389/fnins.2023.1134867.

Sanders, L.M. and Zeisel, S.H. (2007) 'Choline: Dietary requirements and role in brain development', *Nutrition Today*, 42(4), pp. 181–186. doi:10.1097/01.NT.0000286155.55343.fa.

Sarma, M.K. *et al.* (2014) 'Regional brain gray and white matter changes in perinatally HIV-Infected adolescents', *NeuroImage: Clinical*, 4, pp. 29–34. doi:10.1016/j.nicl.2013.10.012.

Sherr, L. *et al.* (2014) 'Developmental challenges in HIV infected children-An updated systematic review', *Children and Youth Services Review*, 45(C), pp. 74–89. doi:10.1016/j.childyouth.2014.03.040.

Smith, S.M. (2002) 'Fast robust automated brain extraction', *Human Brain Mapping*, 17(3), pp. 143–155. doi:10.1002/hbm.10062.

Sohn, A.H. and Hazra, R. (2013) 'The changing epidemiology of the global paediatric HIV epidemic: Keeping track of perinatally HIV-infected adolescents', *Journal of the International AIDS Society*, 16, pp. 1–8. doi:10.7448/IAS.16.1.18555.

Souza, E. *et al.* (2010) 'Long-term follow-up outcomes of perinatally HIV-infected adolescents: Infection control but school failure', *Journal of Tropical Pediatrics*, 56(6), pp. 421–426. doi:10.1093/tropej/fmq008.

Srinivasan, R. *et al.* (2004) 'A comparative study of myo-inositol quantification using lcmodel at 1.5 T and 3.0 T with 3 D 1H proton spectroscopic imaging of the human brain', *Magnetic Resonance Imaging*, 22(4), pp. 523–528. doi:10.1016/J.MRI.2004.01.028.

Stagg, C.J. *et al.* (2013) 'Whole-brain magnetic resonance spectroscopic imaging measures are related to disability in ALS', *Neurology*, 80(7), pp. 610–615. doi:10.1212/WNL.0b013e318281ccec.

Telzer, E.H. *et al.* (2013) 'Meaningful Family Relationships: Neurocognitive Buffers of Adolescent Risk Taking', *National Institute of Health* [Preprint]. doi:10.1162/jocn.

Thompson, P.M. *et al.* (2006) '3D mapping of ventricular and corpus callosum abnormalities in HIV/AIDS', *NeuroImage*, 31(1), pp. 12–23. doi:10.1016/j.neuroimage.2005.11.043.

Toich, J.T.F. *et al.* (2018) 'Functional connectivity alterations between networks and associations with infant immune health within networks in HIV infected children on early treatment: A study at 7 years', *Frontiers in Human Neuroscience*, 11(January), pp. 1–15. doi:10.3389/fnhum.2017.00635.

UNAIDS (2022a) 'Estimates Adults and children living with HIV Country factsheets: South Africa', *Unaids*, pp. 1–6. Available at: https://aidsinfo.unaids.org/%250D.

UNAIDS (2022b) *Global HIV & AIDS statistics - Fact Sheet*. Available at: https://www.unaids.org/en/resources/fact-sheet.

Valcour, V. *et al.* (2012) 'Central nervous system viral invasion and inflammation during acute HIV infection', *Journal of Infectious Diseases*, 206(2), pp. 275–282. doi:10.1093/infdis/jis326.

Wansapura, J.P. *et al.* (1999) 'NMR relaxation times in the human brain at 3.0 Tesla', *Journal of Magnetic Resonance Imaging*, 9(4), pp. 531–538. doi:10.1002/(SICI)1522-2586(199904)9:4<531::AID-JMRI4>3.0.CO;2-L.

Willen, E.J. *et al.* (2017) 'Young adults perinatally infected with HIV perform more poorly on measures of executive functioning and motor speed than ethnically matched healthy controls', *AIDS Care - Psychological and Socio-Medical Aspects of AIDS/HIV*, 29(3), pp. 387–393. doi:10.1080/09540121.2016.1234677.

Wilson, M. *et al.* (2011) 'A constrained least-squares approach to the automated quantitation of in vivo 1H magnetic resonance spectroscopy data.', *Magnetic resonance in medicine : official journal of the Society of Magnetic Resonance in Medicine / Society of Magnetic Resonance in Medicine*, 65(1), pp. 1–12. doi:10.1002/mrm.22579.

Wilson, M. *et al.* (2019) 'Methodological consensus on clinical proton MRS of the brain: Review and recommendations', *Magnetic Resonance in Medicine*, 82(2), pp. 527–550. doi:10.1002/mrm.27742.

van Wyhe, K.S. *et al.* (2021) 'Cognitive outcomes at ages seven and nine years in South African children from the children with HIV early antiretroviral (CHER) trial: a longitudinal investigation', *Journal of the International AIDS Society*, 24(7), pp. 1–14. doi:10.1002/jia2.25734.

Yiannoutsos, C.T. *et al.* (2004) 'Regional patterns of brain metabolites in AIDS dementia complex', *NeuroImage*, 23(3), pp. 928–935. doi:10.1016/J.NEUROIMAGE.2004.07.033.

Young, K. *et al.* (2010) 'Multivariate statistical mapping of spectroscopic imaging data', *Magnetic Resonance in Medicine*, 63(1), pp. 20–24. doi:10.1002/mrm.22190.

Zahr, N.M. *et al.* (2014) 'Imaging Neuroinflammation? A Perspective from MR Spectroscopy', *Brain*

Pathology, 24(6), pp. 654–664. doi:10.1111/bpa.12197.

Zahr, N.M. *et al.* (2020) 'Sensitivity of ventrolateral posterior thalamic nucleus to back pain in alcoholism and CD4 nadir in HIV', *Human Brain Mapping*, 41(5), pp. 1351–1361. doi:10.1002/hbm.24880.

Zeisel, S. (2006) 'The Fetal Origins of Memory: The Role of Dietary Choline in Optimal Brain Development', *J Pediatric* [Preprint]. doi:10.1016/j.jpeds.2006.06.065.

Zeisel, S.H. and Da Costa, K.A. (2009) 'Choline: An essential nutrient for public health', *Nutrition Reviews*, 67(11), pp. 615–623. doi:10.1111/j.1753-4887.2009.00246.x.

Zhang, Y. *et al.* (2018) 'Comparison of reproducibility of Single Voxel Spectroscopy and Whole Brain Magnetic Resonance Spectroscopy Imaging at 3T', *NMR Biomedical* [Preprint]. doi:10.1002/nbm.3898.

Zhang, Y., Brady, M. and Smith, S. (2001) 'Segmentation of brain MR images through a hidden Markov random field model and the expectation-maximization algorithm', *IEEE Transactions on Medical Imaging*, 20(1), pp. 45–57. doi:10.1109/42.906424.